2021

Integrated Geophysical Investigation of Near-Surface Faults - Sassafras Ridge, New Madrid Seismic Zone, USA

Cooper Cearley
University of Kentucky, coopercearley50@gmail.com
Digital Object Identifier: https://doi.org/10.13023/etd.2021.397

STUDENT AGREEMENT:

I represent that my thesis or dissertation and abstract are my original work. Proper attribution has been given to all outside sources. I understand that I am solely responsible for obtaining any needed copyright permissions. I have obtained needed written permission statement(s) from the owner(s) of each third-party copyrighted matter to be included in my work, allowing electronic distribution (if such use is not permitted by the fair use doctrine) which will be submitted to UKnowledge as Additional File.

I hereby grant to The University of Kentucky and its agents the irrevocable, non-exclusive, and royalty-free license to archive and make accessible my work in whole or in part in all forms of media, now or hereafter known. I agree that the document mentioned above may be made available immediately for worldwide access unless an embargo applies.

I retain all other ownership rights to the copyright of my work. I also retain the right to use in future works (such as articles or books) all or part of my work. I understand that I am free to register the copyright to my work.

REVIEW, APPROVAL AND ACCEPTANCE

The document mentioned above has been reviewed and accepted by the student's advisor, on behalf of the advisory committee, and by the Director of Graduate Studies (DGS), on behalf of the program; we verify that this is the final, approved version of the student's thesis including all changes required by the advisory committee. The undersigned agree to abide by the statements above.

Cooper Cearley, Student

Dr. Edward W. Woolery, Major Professor

Dr. Michael M. McGlue, Director of Graduate Studies

Integrated Geophysical Investigation of Near-Surface Faults - Sassafras Ridge, New Madrid Seismic Zone, USA

THESIS

A thesis submitted in partial
fulfillment of the requirements for
the degree of Master of Science in
the College of Arts and Sciences at
the University of Kentucky

By
Cooper S. Cearley
Lexington, Kentucky

Director: Dr. Edward W. Woolery, Professor of Geophysics
Lexington, Kentucky

2021

ABSTRACT OF THESIS

Integrated Geophysical Investigation of Near-Surface Faults - Sassafras Ridge, New Madrid Seismic Zone, USA

The New Madrid Seismic Zone (NMSZ) is a large source of seismic hazard within the central and eastern United States. Seismogenic source parameters such as active fault location, slip rate, total displacement, and strain accommodation is poorly constrained due to the masking effect of the Mississippi Embayment sediment and agricultural practices on structures and surface expressions. Consequently, noninvasive geologic and geophysical investigation of the subsurface is needed to characterize seismogenic sources. Recent investigation of the Reelfoot Fault found that there is a strain accommodation enigma between the dextral offset at seismogenic depth versus the surface expression, Reelfoot Scarp. This strain imbalance was suggested to be due to a dextral shear zone from a splayed portion of the Axial Fault continuing through Reelfoot Fault to the northeast. Seismic reflection surveys collected at Sassafras Ridge, 12 km to the northeast of Reelfoot Fault, found a dextral transpressional structure in Paleozoic to Eocene horizons. This structure was suggested to be an extension of the shear zone to the northeast of Reelfoot Fault but could not satisfy temporal boundary conditions due to the lack of resolution in the upper 50 m. New, near-surface seismic reflection surveys were collected at Sassafras Ridge, targeting the basal Quaternary gravel and intra-Quaternary sediments. The resultant images showed steeply dipping northeast striking faults with vertically offset and arched Quaternary reflectors, extending within 5 m of the surface. There are five imaged transpressional faults within two zones of deformation, forming an ∼600 m wide flower structure, with vertical displacements of 9 m and 4 m at the top of the Quaternary basal gravel, and top of the intra-Quaternary coarse sands, respectively. The seismic images were correlated with LiDAR digital terrain analysis and an electrical resistivity survey to characterize the near-surface extent of these faults. The results suggest that the transpressional flower structure imaged across Paleozoic to Quaternary reflectors extends to the surface and is expressed as a lineament spanning the length of Sassafras Ridge observed in LiDAR slope and roughness maps. These results provide further evidence for the hypothesized shear accommodation fault across the Reelfoot Fault, as well as identifying a previously unknown Quaternary-active fault in westernmost Kentucky, northeast of the most active parts of the NMSZ.

KEYWORDS: Geophysics, Reflection Seismology, Light Distance and Ranging, New Madrid Seismic Zone

Cooper S. Cearley

October 29, 2021

Integrated Geophysical Investigation of Near-Surface Faults - Sassafras Ridge, New Madrid Seismic Zone, USA

By
Cooper S. Cearley

Edward W. Woolery
Director of Thesis

Michael M. McGlue
Director of Graduate Studies

October 29, 2021

ACKNOWLEDGMENTS

The following thesis, while an individual work, benefited from the insights and direction of several people. First, my advisor, Dr. Edward W. Woolery, who exemplified the high quality scholarship to which I aspire. In addition, Dr. Woolery, provided timely and instructive comments and evaluation at every stage of the thesis process, allowing me to complete this project on schedule. Next, I wish to thank the complete Thesis Committee: Dr. Woolery, Dr. Zhengming Wang, and Dr. Jason Dortch. Each individual provided insights that guided and challenged my thinking, substantially improving the finished product. In addition to the technical and instrumental assistance above, I received equally important assistance from family and friends. Thank you to my parents Suzanne and Charles, my brother Griffin, and my friends for continued support, patience, and encouragement through this process. Most importantly, I wish to thank those organizations that made this work possible through generous funding: Department of Energy through the Kentucky Research Consortium for Energy and Environment and specifically Steve Hampson, as well as the Kentucky Geological Survey, and the Dept. of Earth and Environmental Sciences' Ferm Endowment.

TABLE OF CONTENTS

LIST OF TABLES

LIST OF FIGURES

Chapter 1 Introduction

1.1 Problem

The New Madrid Seismic Zone (NMSZ) is generally described as consisting of three main fault segments; two northeast striking dextral fault segments, the Axial (AF) and New Madrid North (NMNF) faults, and a northwest striking central step-over reverse/thrust fault, called the Reelfoot Fault (RF). Previous studies have shown the RF exhibits approximately 12 km of dextral offset at seismogenic depth, but only about 6 km of dextral offset across its surface expression, the Reelfoot Scarp (Pratt et al., 2013). This difference represents a significant strain imbalance for this part of the NMSZ system (Pratt et al., 2013). Pratt et al. (2013) suggested the AF, or part of the AF, may act as a through-going transpressional fault zone cross-cutting the RF as a potential solution for the kinematic discrepancy. (Woolery and Almayahi, 2014) and Greenwood et al. (2016) subsequently found evidence supporting this idea. As part of a general site characterization study at the Central United States Seismic Observatory (CUSSO) located at Sassafras Ridge, Kentucky; Woolery and Almayahi (2014) performed a series of seismic reflection surveys that discovered a zone of transpressional style faults. The location of these subsurface findings is approximately 12 km to the northeast of RF and along the northwest boundary of the Pratt et al. (2013) hypothesized through-going shear zone. Woolery and Almayahi (2014) thus suggested the spatial and architectural consistency of these faults were in agreement with the Pratt (2012) hypothesized through-going shear zone. Additional support for a shear zone piercing point located along RF northwest of Reelfoot Lake was suggested by Greenwood et al. (2016). They searched for right-lateral offset across RF acting as a potential shear-zone piercing, south of Reelfoot Lake at RF's intersection with the AF's Cottonwood Grove (CGF) and Ridgely Ridge (RRF) fault strands.

Pratt (2012) and Greenwood et al. (2016) originally thought this location was the most likely piercing point; however, the Greenwood et al. (2016) results showed no right-lateral strike-slip movement of the RF across the CGF and RRF, thus suggesting that any piercing point was likely further to the northwest along the strike of RF, northwest of Reelfoot Lake (Odum et al., 1998; Pratt et al., 2013; Woolery and Almayahi, 2014). Rosandich (2019) subsequently completed seismic reflection surveys located northwest of Reelfoot Lake, along the northwestern limits of the hypothesized shear zone (Pratt et al., 2013), near the community of Proctor City, TN. Their results showed near-vertical, transpressional styled faults offsetting Paleozoic through Quaternary horizons, leading to interpretations that were similar to those made by Woolery and Almayahi (2014), but clearly indicated fault displacement into the late Quaternary. This was interpreted as a primary candidate for the piercing point of the shear zone, which is important because it would define where a transpressional shear zone splay of the AF cross cuts the RF. The Woolery and Almayahi (2014) findings were along the projected strike of the Rosandich (2019) structures; however fault displacement was confined along the base of the Quaternary horizon, making late-Quaternary activity equivocal. The acquisition array aperture, which was desgined for depths between 0.1 and 0.6 km, prevented their P-wave surveys from imaging the upper 50 m of the subsurface. To determine if the faults imaged at Sassafras Ridge are a continuation of the transpressional faults imaged across the RF, late-Quaternary displacement must be demonstrated to satisfy the temporal boundary conditions. Consequently, this thesis investigates spatial and temporal characteristics of the near-surface (<50 m) using SH-wave mode seismic reflection methods to target potential fault deformation within the intra-Quaternary sediments. The SH-wave reflection data were collected coincident with structure anomalies found in the Woolery and Almayahi (2014) P-wave surveys UK-1 and UK-1a. A previously collected and collocated electrical resistivity (ER) profile used for assessing the site

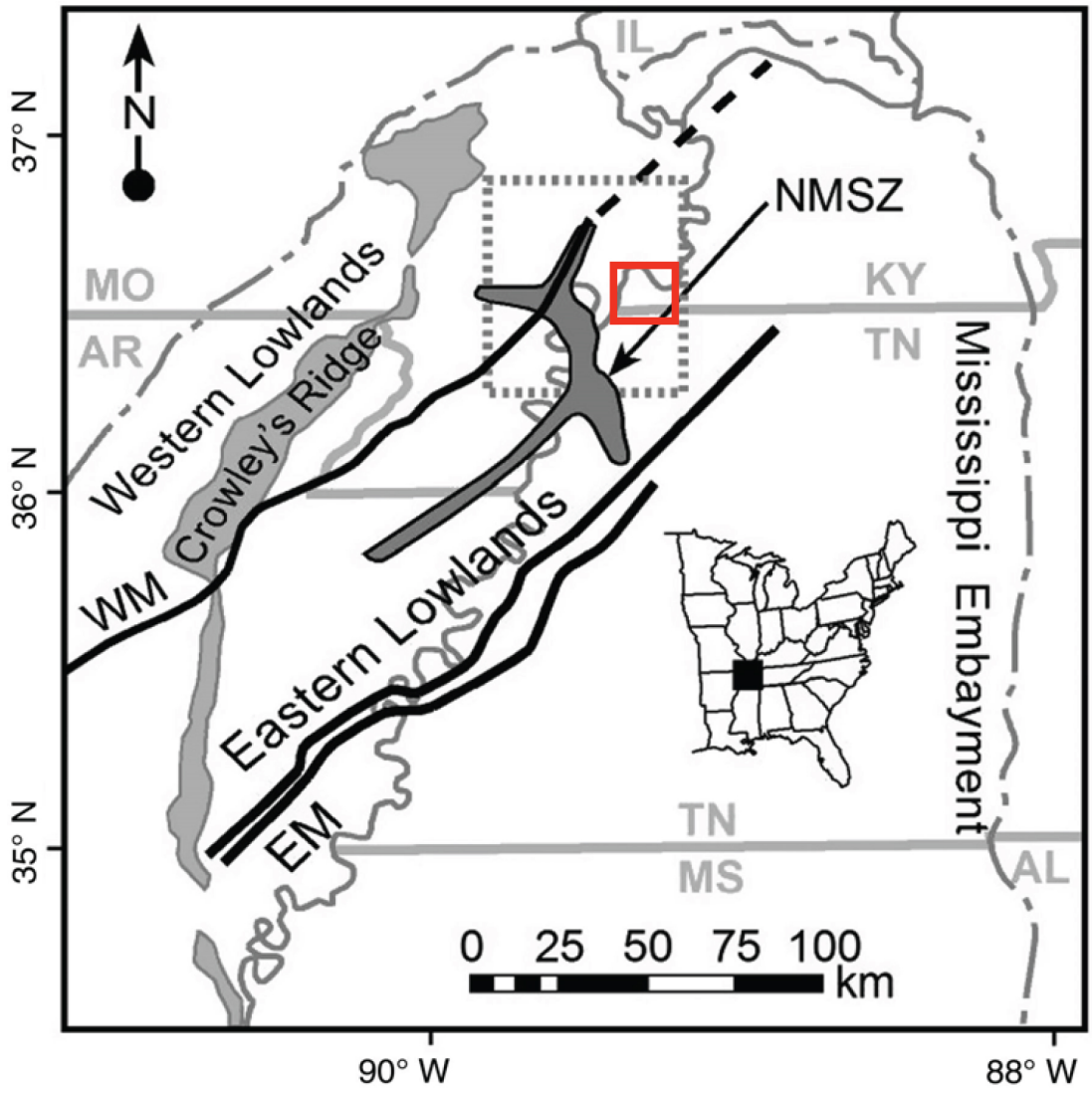

Figure 1.1: Location of New Madrid Seismic Zone. Earthquake epicentral pattern is depicted by the dark grey zone. The southwestern arm is representing Axial Fault, while the central, northwestern oriented segment is the RF. The gray dashed box depicts the region shown in Figure 1.3, while the red box shows the approximate region shown in Figure 3.7 and 3.6. From Csontos and Van Arsdale (2008), modified from Woolery and Almayahi (2014).

hydrostratigraphy was also incorporated into the fault assessment (Cooper, 2016). Additionally, high-resolution digital terrain analysis with Light Detection and Ranging (LiDAR) datasets were utilized to evaluate the site geomorphology and potential surface manifestation of faults imaged at depth by Woolery and Almayahi (2014).

1.2 Hypothesis

The northeast-striking transpressional faults imaged by Woolery and Almayahi (2014) are hypothesized to be Quaternary active and a part of a suggested northeast oriented shear zone accommodating a strain imbalance across a piercing point with the RF, located approximately 12 km to the southwest. The extension of deformation into the Quaternary is a required, but still unproven, temporal boundary condition for the kinematic strain-accommodation structure associated with a northeast projected AF shear zone. Without an older, but still active dextral fault, an accommodating through-going shear is not possible. Understanding if near-surface deformation extends into the late-Quaternary sediments will satisfy the temporal element for the Sassafras Ridge faults as a viable northeastern extension of the dextral strike-slip fault zone (AF).

1.3 Objectives and Significance

The NMSZ largely controls the seismic hazards in the central U.S.A. (Frankel, 1995). The NMSZ experienced a series of at least three large earthquakes between December, 1811 and February, 1812. These earthquakes were estimated to range between 7.6 and 8.0 moment magnitude (Nuttli, 1973; Johnston and Schweig, 1996). The resultant earthquake groundmotions from the 1811-1812 sequence were described to have an "unusually large felt area" (Nuttli, 1973). Nuttli (1973) and Johnston and Schweig (1996) noted that ground-shaking and felt effects from the main-shock events, based the Modified Mercalli Intensity scale, reached as far as the Atlantic Coast, with intensities of a V. While the NMSZ serves as a significant area for central U.S.A seismic hazards (Frankel, 1995), certain mechanisms such as slip rate, total displacement, strain accommodation, and Quaternary-active fault locations are still ambiguous across certain parts of the NMSZ system (Pratt, 1994; Schweig and Ellis,

1994; Johnston and Schweig, 1996; Newman et al., 1999; Cox et al., 2000; Van Arsdale, 2000; Tuttle et al., 2002; Calais et al., 2005; Smalley et al., 2005; Calais and Stein, 2009; Calais et al., 2010; Pratt, 2012; Pryne et al., 2013).

Traditionally, invasive drilling and non-invasive geophysical imaging methods have been required to provide better subsurface definition within the NMSZ system. Recent introduction of LiDAR digital terrain analysis provides additional landscape detail. Due to fewer numbers of subsurface investigations in the area, and lack of availability of LiDAR until recently, hazard parameters northeast of the NMSZ's highly active RF are presently even less constrained. Woolery and Almayahi (2014) collected near-surface P-wave seismic reflection profiles (UK 1 and UK 1a; Figure 1.2) approximately 12 km northeast of the RF step-over and in-strike with the AF and within the boundaries of the hypothesized through-going shear zone (Pratt, 2012). Their results imaged near-vertical, N30E striking faults showing uplifted and arched post-Paleozoic sediments, consistent with transpressional, dextral faulting. More significantly, the new 12 km inclusion is geographically and kinematically coincident with the proposed northeast continuation of the NMSZ's southern Axial shear zone across the RF, providing an accommodation solution for differential strain on RF (Odum et al., 1998; Pratt, 2012; Pryne et al., 2013). Consequently, this study is coincident with the UK 1a P-wave survey (Woolery and Almayahi, 2014) and targets the potential extension of the Sassafras Ridge faults into the Quaternary sediments. We used the UK-1a survey to target structures for the SH-wave seismic reflection survey and surficial LiDAR analysis to better constrain the fault style, near-surface extent, and possible surface exposure of the hypothesized shear zone extension.

Confirmation of the project hypothesis will provide additional evidence for resolving the long-standing strain accommodation enigma associated with the RF, and a con-

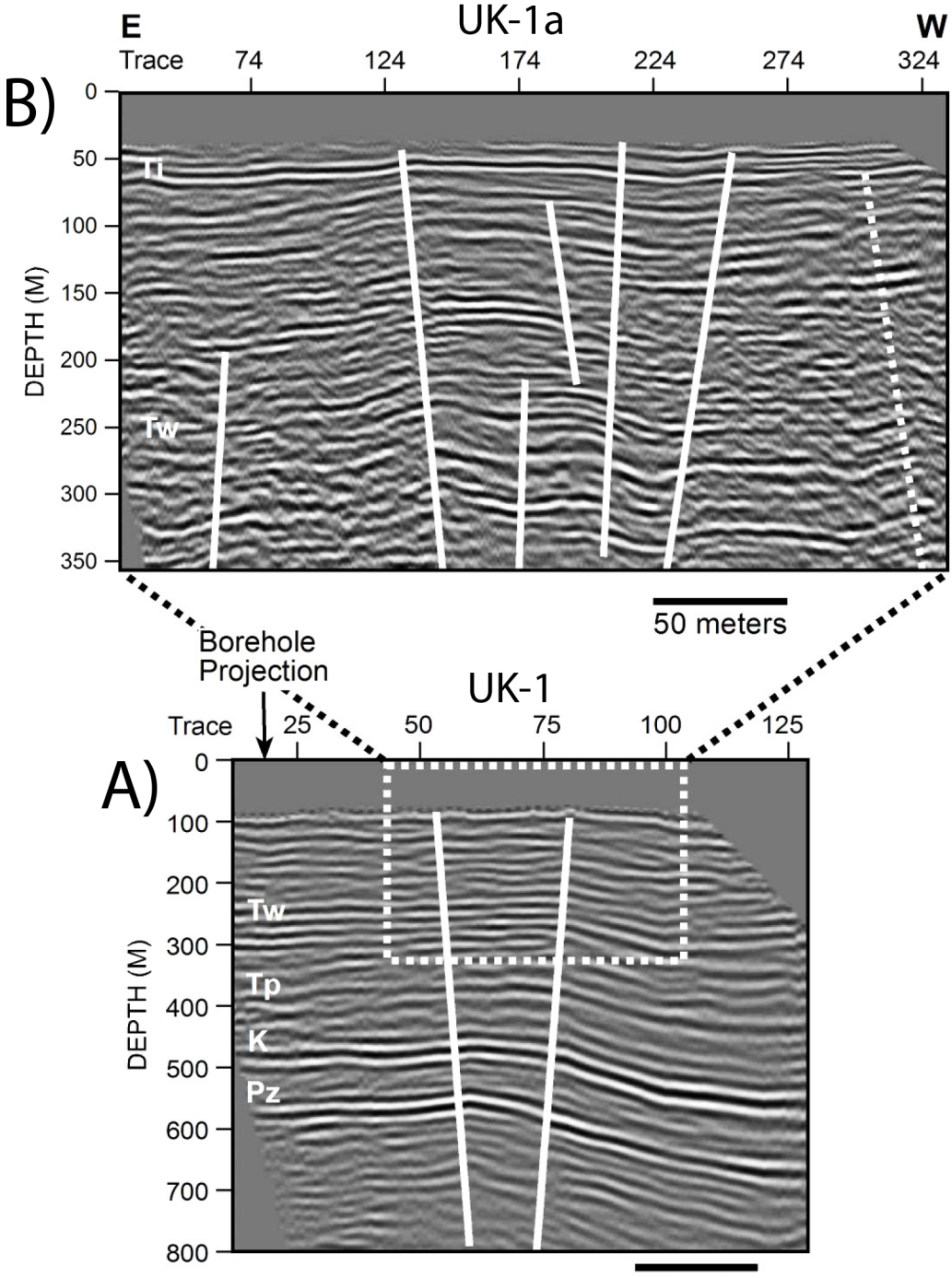

Figure 1.2: P-wave seismic reflection profiles collected by Woolery and Almayahi (2014) at Sassafras Ridge. Figure shows the spatial relationship between two P-wave surveys collected. Line UK-1a (B) was collected with a smaller array spacing to target the white dashed box depicted in UK-1 (A). Interpretations present were made by Woolery and Almayahi (2014).

ceptual leap in our understanding of the seismotectonic kinematics for the intraplate, transpressional seismic zone in general. Positive hypothesis results will also reduce the uncertainty in seismic hazard assessment in the central U.S.A by identifying unknown Quaternary active faults and the spatial extension of a larger through-going fault zone. This work will also correlate near-surface seismic reflection (SH-wave) with newer digital terrain analysis methods across the Sassafras Ridge. Additionally, previously collected P-wave reflection surveys will be correlated with near-surface profiles, completing the characterization of the fault mechanisms for Paleozoic stratigraphy to the surface or near surface. This project will assess the potential for unidentified Quaternary-active faults in the central U.S.A, as well as provide spatial and temporal parameters for future fault modeling. Specific tasks to achieve thesis objective are included:

1. Collection, processing, and interpretations of 0.6 km of high-resolution, near-surface SH-wave seismic reflection data coincident with the P-wave survey collected by Woolery and Almayahi (2014). These data are used to constrain attitude, deformation style, spatial and temporal characteristics of near-surface structure associated with the Sassafras Ridge faults.

2. Completion of terrain analysis using LiDAR datasets to relate geomorphic surface anomalies to subsurface fault structure, thus providing a relative time constraint.

3. Correlation of new seismic reflection data with previously collected near-surface electrical resistivity (ER) data (Cooper, 2016) and LiDAR analysis to evaluate temporal extent of fault deformation. As well as to investigate near-surface deformation within the Quaternary to determine active faulting within the hypothesized through-going shear zone.

1.4 Tectonic Setting

The NMSZ is an intraplate seismic setting located in the northern Mississippi Embayment. The extent of the NMSZ spans across multiple states (i.e. Kentucky, Tennessee, Missouri, Arkansas). The seismic zone is historically known for a series of 7+ magnitude earthquakes in the winter of 1811-1812 (Nuttli, 1973; Herrmann and Canas, 1978; Johnston and Schweig, 1996). The main sequence of shocks lasted 8 weeks and at least three major earthquakes have been estimated to be approximately 7.5 in moment magnitude (Johnston and Schweig, 1996). The NMSZ contains multiple tectonic structures that have been investigated by geologists and geophysicists, such as Reelfoot Rift, Bylthеville Arch, and the Tiptonville Dome (Ervin and McGinnis, 1975; Crone, 1998; Parrish and Van Arsdale, 2004; Greenwood et al., 2016). The host structure of the seismic zone is the Reelfoot Rift and formed in late Proterozoic to early Cambrian times. The Reelfoot Rift is expressed as a 300-km-long, 70-km-wide graben formed as a failed rift, or an aulacogen, off the margin of the opening Iapetus Ocean (Ervin and McGinnis, 1975; Crone, 1998). Common with mid-continental rifting, there is evidence of magmatic intrusion along the axis of the Reelfoot Rift. The axial magmatic intrusions were interpreted by Rhea and Wheeler (1994), as well as Langenheim (1995) through aeromagnetic data (Rhea and Wheeler, 1994; Langenheim, 1995). The largest intrusion is the Bloomfield Pluton (BP) along the northwest rift margin of the Reelfoot Rift. BP is situated at the northwest end of the RF stepover and the southwest end of the New Madrid North Fault. BP is associated with a halo of seismicity where these faults intersect and seismic epicentral locations patterns shows seismicity occurring along the southeastern boundary of the pluton. These magmatic intrusions utilize weak areas in the rock medium, typically using existing fault structures, and are thought to influence subsequent faulting in the region (Langenheim, 1995; Johnston and Schweig, 1996). Another key feature in the seismic zone is the Blytheville Arch, first identified in seismic reflection data by Howe and

Thompson (1984) (Howe and Thompson, 1984; Crone et al., 1985). This structure is defined by a 10-15 km wide zone of up warping Paleozoic reflectors and is centered along the axis of the Reelfoot Rift. Flat-lying continuous strata, Late Cretaceous in age, are positioned on top of the upwarp (Johnston and Schweig, 1996; Crone, 1998). The mechanism for the upwarp is still debated, however, positive flower structures are one mechanism that can produce long, linear upwarping of strata and have been imaged within the region. A positive flower structure indicates strike-slip faulting with a component of compression across the fault (Harding, 1985). Consequently, Blytheville Arch formed during a period of transpressional strike-slip faulting along preexisting, reactivated axial faults (Johnston and Schweig, 1996).

The seismically active portion of the NMSZ is composed of three major fault segments; two northeast-oriented dextral strike-slip fault zones (AF and NMNF) connected by a northwest striking central step-over (RF) (Figure 1.1) (Chiu and Johnston, 1992; Pratt, 1994; Pratt et al., 2013; Woolery and Almayahi, 2014). The RF has been defined as a reverse/thrust fault accommodating deformation from the bounding dextral fault planes, resulting in major topographic uplift in areas such as the Tiptonville Dome (Pratt, 1994). The strike of the RF changes direction around the intersection with the AF zone, which Chiu and Johnston (1992) described as segmenting the Reelfoot Scarp into two planes; the Reelfoot North and Reelfoot South (Chiu and Johnston, 1992). The assumption of a simple three-armed fault zone has been utilized in prior work, however the spatial and physical characteristics that drive seismicity and influence slip rate, displacement, and strain accommodation are still quite ambiguous (Pratt, 1994; Schweig and Ellis, 1994; Johnston and Schweig, 1996; Newman et al., 1999; Cox et al., 2000; Van Arsdale, 2000; Tuttle et al., 2002; Calais et al., 2005; Smalley et al., 2005; Calais and Stein, 2009; Calais et al., 2010; Pratt, 2012; Pryne et al., 2013). This is in large part due to the masking effect of the Mis-

sissippi Embayment sediments on seismogenic exposure. Additionally, this location has a significant amount of agriculture, reworking the surface and removing any seismogenic surface expressions that may have existed. A certain enigma in the NMSZ system is the RF, which has been observed to have approximately 11 km of offset at seismogenic depth, compared to the 5.5 km of topographic offset across the Reelfoot Scarp (Figure 1.3). This difference in offsets presents a strain imbalance across the RF and AF intersection. Several studies suggest a northeastern extension of the AF shear zone through RF exists, accommodating a significant amount of strain (Pratt, 1994; Pratt et al., 2013; Woolery and Almayahi, 2014; Greenwood et al., 2016), but lack substantial field evidence due to a lack of geomorphic and geophysical mapping in the area northeast of the RF.

Pratt (2012) published an investigation of RF employing computational models to show the RF is a restraining stepover fault structure. These models attempt to predict modern seismicity in the NMSZ from comparison with analogous sandbox model simulations. These models suggested that the accommodation of modern seismicity only occurs on a subset of faults, where the trends of younger faults seem to match with the direction of shearing, supporting the idea for a possible shear zone. Additional support came from Odum et al. (1998) published study that interpreted a subset of parallel northeast-trending tear faults that seem to partition the hanging wall of the RF thrust into subparallel blocks (Figure 1.4). Their study presented atleast 5 faults (F1-F5) that interact with the RF step-over, each one seemingly coincident with a bend in the fault plane. These faults were determined through a variety of geophysical investigations; F1 was originally identified by Hamilton et al. (1982). F2-F5 were delineated by Odum et al. (1998) through a variety of seismic reflection methods. Odum et al.'s findings suggested the faults are deep rooted and could be structurally related to the seismicity patterns observed throughout the NMSZ sys-

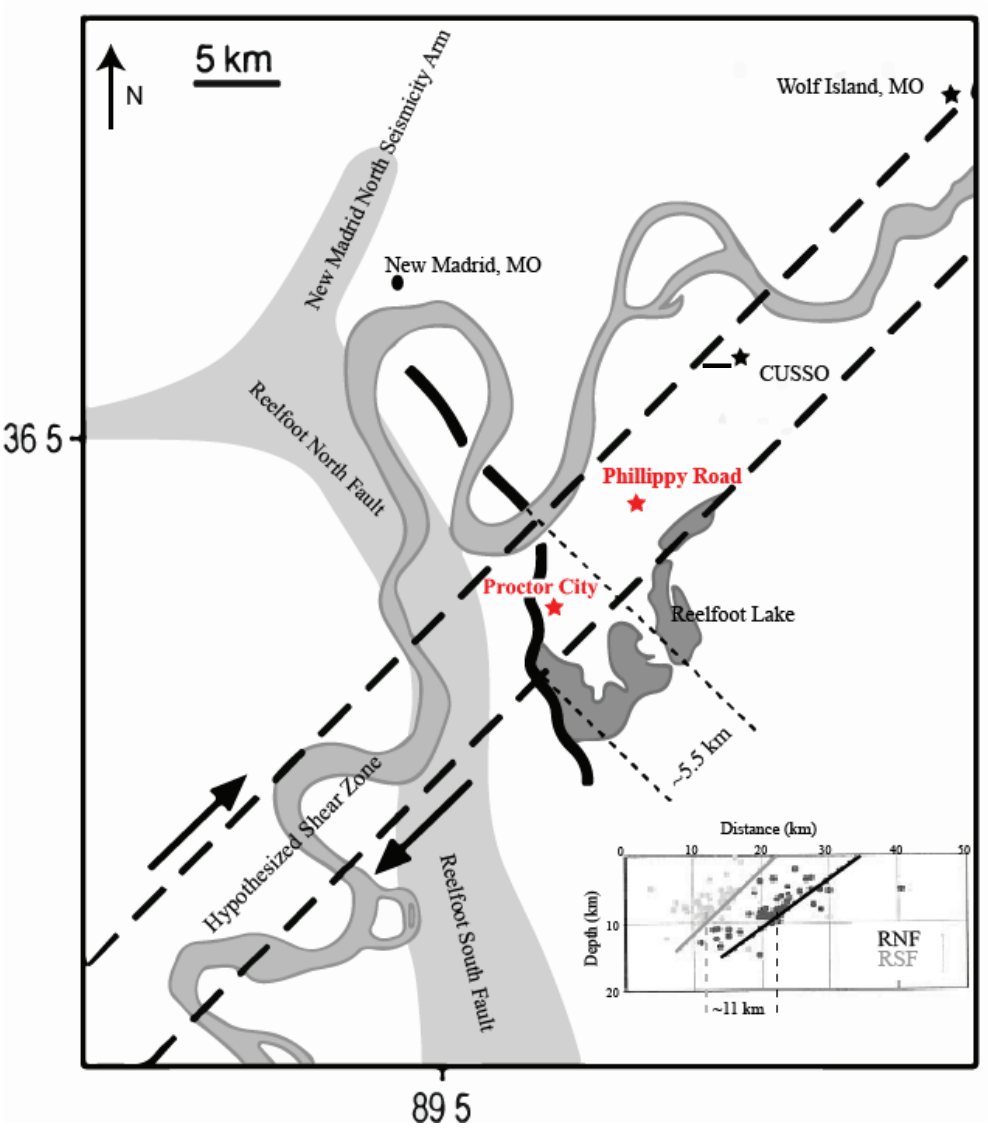

Figure 1.3: Map of the Central NMSZ, modified from Pratt et al. (2012), showing the hypothesized shear zone extension northeast of the RF. Red stars depict locations of previous studies investigating the shear zone extension piercing point (Rosandich, 2019). Black star shows the location of the Central United Stated Seismic Observatory (CUSSO) borehole, as well as the location of a previous study (Woolery and Almayahi, 2014), as well as the location of this study. Wolf Island identifies the location of a large scale industry seismic profile collected by DOW Chemical. The Reelfoot Scarp (solid black line) shows approxiamately half the dextral offset than that present as seismogenic depth (lower right-hand box). Pratt (2012) and Woolery and Almayahi (2014) suggest the hypothesized shear zone continues northeast, likely between the heavy black dashed lines.

tem. The CGF and RRF, towards the southern extent of RF, was speculated to be a possible site of strike-slip faults cross-cutting the RF. Greenwood et al. (2016) investigated the CGF and RRF for a piercing point of AF through RF. If found, they hypothesized that dextral faults could balance the strain discrepancy seen across the RF. However, their results showed that there was no right-lateral displacement of the RF across the CG and RR faults, thus suggesting any piercing point was further to the northwest, along strike of the RF, possibly at the intersection of a splayed part of the AF and RF which had been proposed by other studies (Odum et al., 1998; Csontos and Van Arsdale, 2008; Csontos et al., 2008; Pratt, 2012; Woolery and Almayahi, 2014).

Rosandich (2019) hypothesized the piercing point for the shear zone through RF was at the small community of Proctor City, TN, to the northwest of Reelfoot Lake, based on anomalous surficial offset in the Reelfoot Scarp. This location is coincident with the strike of the AF, and the segmentation of the RF into the RF North and RF South (Chiu and Johnston, 1992). Rosandich (2019) presented results that indicate a Quaternary-active, transpressional fault zone of the AF across RF. This piercing of the AF through RF is a 500-m-wide zone of transpressional faults displacing intra-Quaternary sediment, imaged with both P-wave and SH-wave reflection surveys. The results also showed faults that displaced the basal Quaternary by 5-7 m. Additionally, the faults imaged depicted warped and offset reflectors across the Eocene and Quaternary horizons, as well as antiforms between faults due to the transpressional strain. The structure of the faults and associated deformation is consistent with a transpressional flower structure. Results from Rosandich (2019) provided a possible solution to the strain imbalance seen across RF, and indicated that the AF has continuously accommodated right-lateral displacement through time; with only a small portion of the motion being represented by vertical displacement of the RF (Pratt,

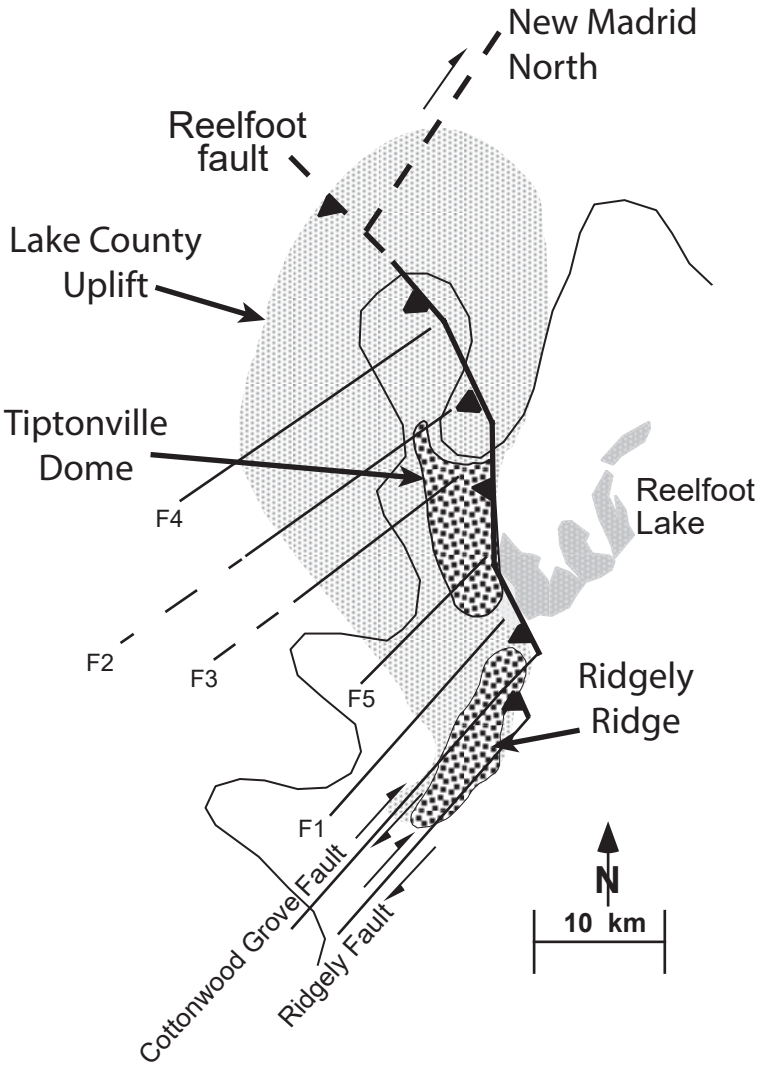

Figure 1.4: Schematic of the Reelfoot thrust fault showing inferred locations of northeast-trending faults that are thought to partition the hanging wall of the thrust by Odum et al. (1998). Lines denoting F1-F5 are faults. The CG and F1 faults lie within the Blytheville fault zone (Johnston and Schweig, 1996). Modified from Odum et al. (1998).

2012; Rosandich, 2019). Rosandich et al.'s (2019) Proctor City, TN and Phillipy, KY fault interpretation projects along strike with the Woolery and Almayahi (2014) transpressional structures at Sassafras Ridge, 12 km northeast of the central step-over; extending the Axial shear zone to the northeast 12 km. (Woolery and Almayahi, 2014; Rosandich, 2019). Woolery and Almayahi (2014) completed their study utilizing near-surface P-wave reflection methods and correlated with local large-scale, industry seismic reflection profiles at Wolf Island, MO. Correlation with the industry profile suggests the possibility of a further extension of this transpressional structure 34 km further to the northeast, however without evidence that satisfies the late-Quaternary temporal boundary condition, this is equivocal. Woolery and Almayahi's results presented near-vertical, transpressional faults and (lines UK-1 and UK-1a)(Figure 1.2) warped and offset reflectors from the Paleozoic to basal Quaternary horizons. While Woolery and Almayahi's (2014) results were along the projected strike of Rosandich et al. (2019) structures, fault displacement was confined to the basal Quaternary horizon, making late-Quaternary interpretations equivocal. It has been noted that evidence for dextral faults, striking approximately N30E, displacing Quaternary sediments would provide more support for a possible solution to the strain imbalance problem across NMSZ (Pratt et al., 2013); where strain is accommodated through a series of step-over strike-slip faults. The accommodation of strain across a series of faults rather than a single fault (RF) would result in the differential offset seen at seismogenic depth versus the surface expression.

1.5 Stratigraphy of the New Madrid Seismic Zone

The stratigraphy of the northeastern Mississippi Embayment is constrained by boreholes. The Central United States Seismic Observatory borehole (CUSSO), which penetrates 587 m to the bedrock, is located adjacent to the UK-1b line presented here, and is used as a control for both velocity analysis and interpretations of stratig-

raphy (Figure 1.5, Table 1.1)(Woolery et al., 2016). The bedrock in the NMSZ is the Ordovician Knox super-group carbonate and the contact meets the Late Cretaceous McNairy sands, at 585 meters depth (Van Arsdale and TenBrink, 2000). This unconformity appears as a strong reflection in seismic data (Woolery and Almayahi, 2014). The McNairy sands and clay is a formation 85 meters thick and appears at a depth of 500 meters. Another unconformity, moving up the section, lies between the McNairy Sands and the Paleocene Porter's Creek Clay formation (Van Arsdale and TenBrink, 2000; Rosandich, 2019). The Porter's Creek Clay formation is ∼100 meters thick, depending on the locale, with the top of the clay formation reaching ∼400 meters in depth. The Eocene Wilcox Group, which consists of sands, silts, and clays, overlays the Paleocene formation and is ∼150 meters thick. The Claiborne Group (Eocene) sits atop the Wilcox Group and consists of groups of sands, silts, and clay sediments. The Claiborne Group is approximately 150 meters thick and encounters the Eocene Jackson formation at ∼130 meters depth. The Eocene Jackson formation contains alternating layers of sands, silts, and clays, up to ∼50 meters depth. The top of the ∼90-meter-thick Jackson formation meets the Quaternary Mississippi River Alluvium and marks another unconformity (Van Arsdale and TenBrink, 2000). The Quaternary Alluvium can be differentiated by its gravelly base and varying grain size sands, silts, and clays reaching all the way to surface (Woolery et al., 2016). The Quaternary Alluvium is ∼50 meters thick and is the target formation for the seismic reflection data presented herein.

The Quaternary Alluvium consists of a large grain gravelly base, which is another strong reflector for regional seismic reflection surveys (Woolery et al., 1993; Harris, 1996; Woolery et al., 1996; Van Arsdale and TenBrink, 2000; Woolery and Almayahi, 2014). Within the Quaternary sediments the layers can be broken down further depending on the grain size of the gravel and sands present. The Quaternary

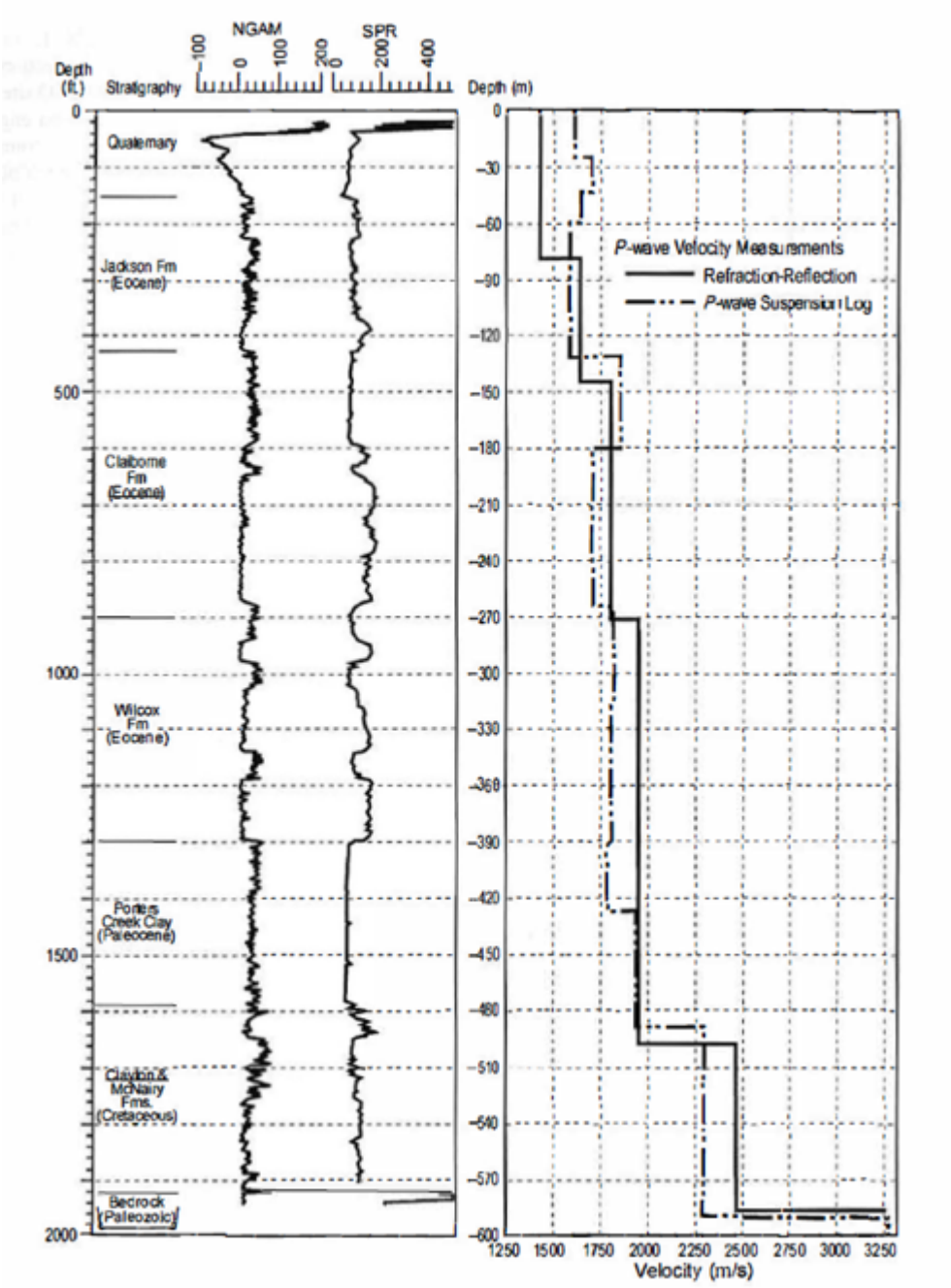

Figure 1.5: Stratigraphic and geophysical well-log interpretations from the CUSSO borehole are shown on the left side of the figure. Self-potential resistivity (SPR), natural gamma (NGAM), and borehole velocity measurements were made. From Woolery and Almayahi (2014).

Table 1.1: General stratigraphy of the northeast New Madrid Seismic Zone, modified from Van Arsdale and TenBrink (2000)(Van Arsdale and TenBrink, 2000; Woolery et al., 2016; Wang and Carpenter, 2019).

Formation Name	Age	Thickness (m)	Depth to top(m)
Unit 3 - Fine brown sand	Quaternary	10	-
Unit 2 - Coarse red and blue sand	Quaternary	20-25	10
Unit 1 - Coarse sand and large gravel	Quaternary	10-15	35
Jackson Formation	Eocene	90	50
Claiborne Group	Eocene	150	140
Wilcox Formation	Eocene	110	290
Porter's Creek Clay	Paleocene	100	400
Clayton-McNairy Formations	Cretaceous	85	500
Knox Supergroup/Bedrock	Ordovician	-	585

stratigraphy is presented in Table 1.1 and is used as a control for the seismic interpretations. The first distinction made within the Quaternary is classified as Unit 1 and consists of primarily coarse sand and large gravel, is 10-15 m thick, and likely represents the basal gravel of the Quaternary Alluvium. Unit 1 contains diffraction patterns in the seismic data, possibly originating from the large gravel lenses. Unit 2 is a $\sim$20 meters thick layer of coarse-grain red and blue sands (Wang and Carpenter, 2019). This layer of sands reaches to roughly 10 meters depth. Unit 3 is the fine-grained sand and topsoil, and is approximately 10 meters thick depending on locale (Woolery et al., 2016).

Chapter 2 Methods

2.1 Reflection Seismology

Reflection seismology utilizes elastic waves generated from a input of energy (e.g., dynamite, shotgun blast, Vibroseis, Thumper, hammer impact) into the ground to create a profile of the subsurface. Sources vary from controlled frequency sources which input energy over a range of frequency (i.e. Vibroseis, Sosie), to impact sources (i.e. hammer, dynamite, shotgun) that releases energy as an impulse. The source generates a wave front that propagates radially outward in the form of seismic waves. Wave attributes such as frequency, amplitude and travel time are recorded by an array of geophones placed at known distances from the source. With known distances and travel times, the velocity of the waves can be determined as they propagate through a geologic medium. The information contained in the waveform can inform the observer of the presence and magnitude of elastic contrasts. When seismic waves traveling through the subsurface encounter a formation of rock or sediment with a different acoustic impedance, energy of the wave-front may be lost, or attenuated through geometric spreading, scattering, partitioning, or absorption (Sheriff and Geldart, 1995; Lillie, 1999; Burger et al., 2006). Energy of a wave-front can also be diffracted when encountering an impedance contrast that is discontinuous (i.e. faults or non-planar horizons).

Seismic waves consist of body waves (P-waves and S-waves) and several types of surface waves. S-waves are transverse waves, propagating with particle motion perpendicular to the direction of the wavefront (Figure 2.1). S-waves can be broken down into key directional components whenever they are polarized in a certain direction, either vertical (SV) or horizontal (SH) polarization (Sheriff and Geldart, 1995).

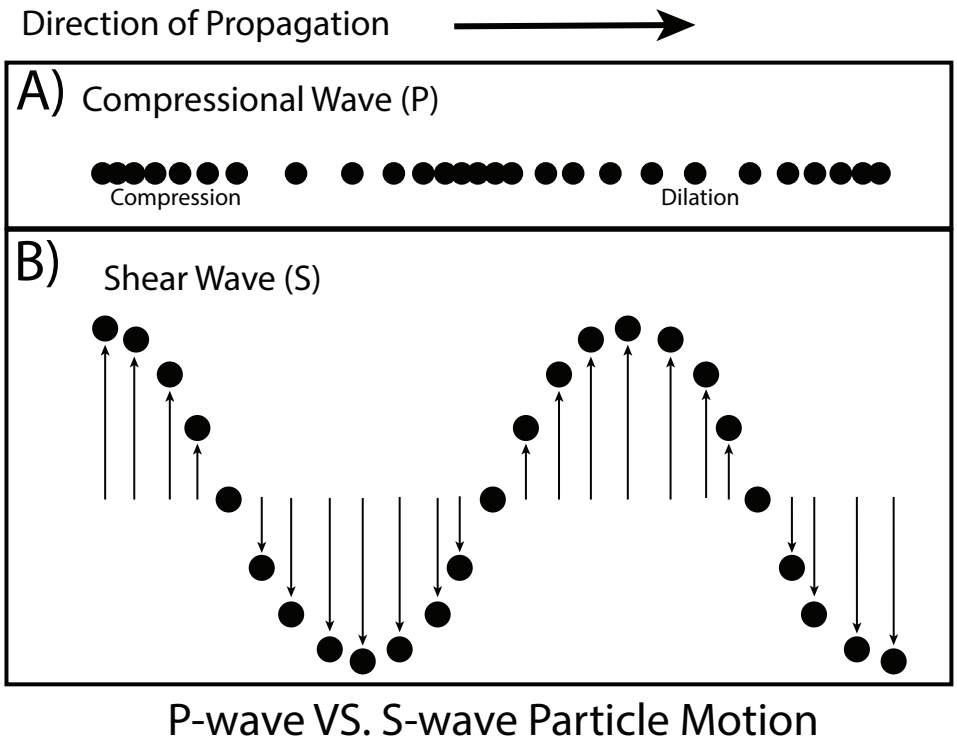

Figure 2.1: Diagram showing different propagation of particles for (A) P-waves and (B) S-waves. Modified from earthquake.usgs.gov.

SH-waves specifically, hold a large advantage when used in near-surface geotechnical applications due to the fact they are "framework waves", propagating through geologic mediums sampling the lithology in water saturated environments (Woolery et al., 1993, 1996; Harris, 1996). SH-waves also have a larger optimum window due to the slower propagation velocities, which allows for easier identification of different events in the recordings (Woolery et al., 1993). The slower velocity of an SH-wave coupled with a smaller wavelength allows for higher resolution data to be acquired when considering resolvable limit and vertical resolution. SH-wave methods offer resolution in water saturated sediments of up to 2-3 times that of P-wave methods (Woolery and Street, 2002). This increased resolution in shallow, water-saturated subsurface in the NMSZ is advantageous due to the small offsets of faults in the near-

surface (Woolery et al., 1993, 1996; Harris, 1996). However, this higher resolution comes at the sacrifice of penetration depth of the signal. SH-waves travel with a higher frequency, but because subsurface material acts as a high-cut filter, SH-wave energy is heavily attenuated and absorbed the further it travels into the subsurface. Resolution refers to the minimum distance in space or time to distinguish two different features (Sheriff and Geldart, 1995). The vertical resolution is determined through Rayleigh's quarter-wavelength criteria ($\lambda/4$), where features in the subsurface must be separated by atleast a quarter of the dominant wavelength to be resolvable as two features rather than one (Widess, 1973). Single features smaller than the resolvable limit are still detectable due to the threshold of detection being $\lambda/20$ to $\lambda/30$, however, thin features, while they may show up on the seismogram, have an indeterminable thickness (Widess, 1973). Due to the vertical resolution being a factor of wavelength, which is determined through a function of velocity divided by frequency, higher frequency data will typically yield higher resolution data. While P-waves can have high frequencies, they also travel at much higher velocities compared to S-waves. Whereas, SH-waves travel with a slower velocity and may have a wavelength of one half or one third that of P-waves (Sheriff and Geldart, 1995; Yilmaz, 2001), resulting in a much higher vertical resolution.

The most common type of reflection survey conducted is known as the common midpoint method (CMP), also referred to as the common depth point (CDP) (Lillie, 1999; Sheriff and Geldart, 1995). The CMP method allows for sampling redundancy, also known as "fold", by collecting traces of reflecting signals gathered from the same subsurface points along various source-to-receiver paths. The compilation of corresponding traces for each point in the subsurface are known as a CMP gather (Lillie, 1999; Baker, 1999). Fold is the amount of times a single subsurface point is sampled and can be expressed by the following relationship:

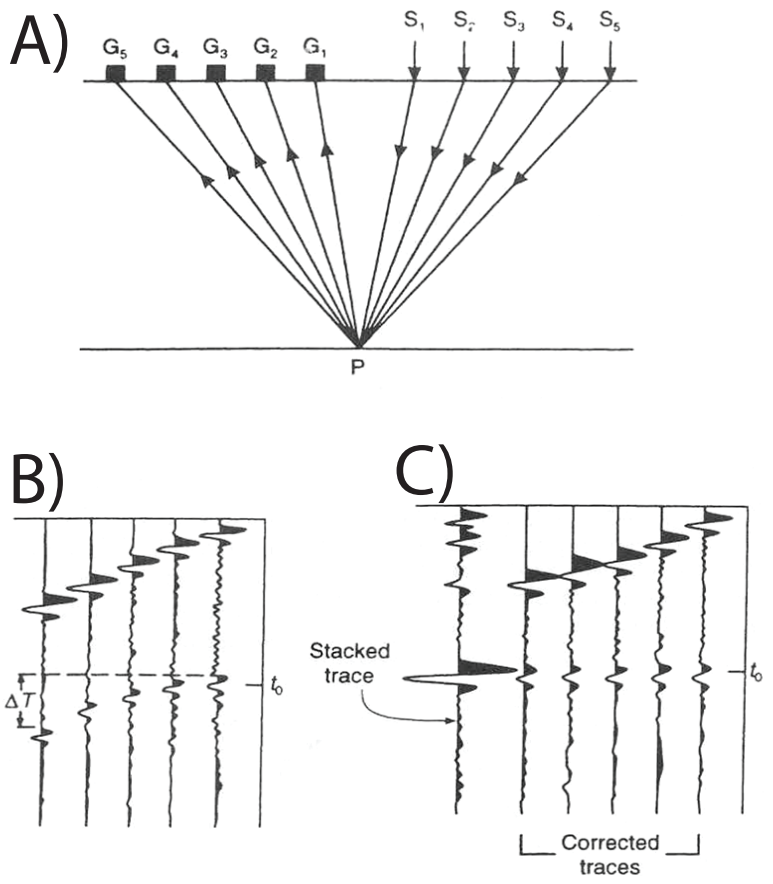

Figure 2.2: Diagram showing the CMP method of a reflection survey. A) is field acquisition of CMP data. B) shows the CMP gather. C) shows NMO corrected gather and then a stacked trace of all the NMO corrected traces. Modified from Burger et al. (2006).

$$Fold = \frac{ReceiverSpacing * Numberof Receivers}{2 * shotspacing} \tag{2.1}$$

This redundancy of information, when combined into a stacked profile, promotes constructive combination of reflections and the elimination of the stochastic, unwanted signal or noise (Burger et al., 2006; Lillie, 1999). The various paths will have varying two-way travel times which must be corrected to a zero-offset time or vertical incidence time. This correction utilizes the normal-moveout (NMO) time shift deter-

mined from a function of the velocity model and source-to-receiver offset. The various ray paths from multiple shot points, corresponding to the same subsurface point, are all recorded at different travel times. When plotted on a graph of trace vs. travel time, a single reflection boundary resembles a hyperbola, with travel time increasing with trace number. This variance in travel time across the reflector is referred to as the normal move-out (NMO) and must be corrected before the traces can be stacked together (Burger et al., 2006; Lillie, 1999; Sheriff and Geldart, 1995). This correction involves bringing all the traces from their position in the NMO hyperbola, to a position of vertical incidence (Baker, 1999); bringing the curved hyperbolic reflection up to zero-offset time (vertical incidence). This correction is done by utilizing the source-receiver offset and the equation for NMO time. A collection of NMO corrected traces is combined to create a stacked profile, showing a 2D cross-sectional view of the subsurface.

2.1.2 Optimal Window

For the most success when collecting near-surface SH-wave reflection data, recording the reflection within the optimum window is required (Hunter et al., 1984). To acquire data within the optimum window, this requires the array of geophones to be place at a distance from the receiver so that key reflections are observed with minimum coherent noise or interference from other arrivals (Hunter et al., 1984). With reflection surveys, near vertical offset is ideal due to the degradation of signal-to-noise ratio through phase reversals, lowering of frequency content, and amplitude anomalies that occurs with wide-angle reflections (Harris, 1996).

SH-wave surveys of unlithified sediments have the optimum window typically come in below the Love wave arrival and at near source-to-receiver offsets (Woolery et al., 1996; Harris, 1996). In order to avoid the negative effects such as wavelet phase,

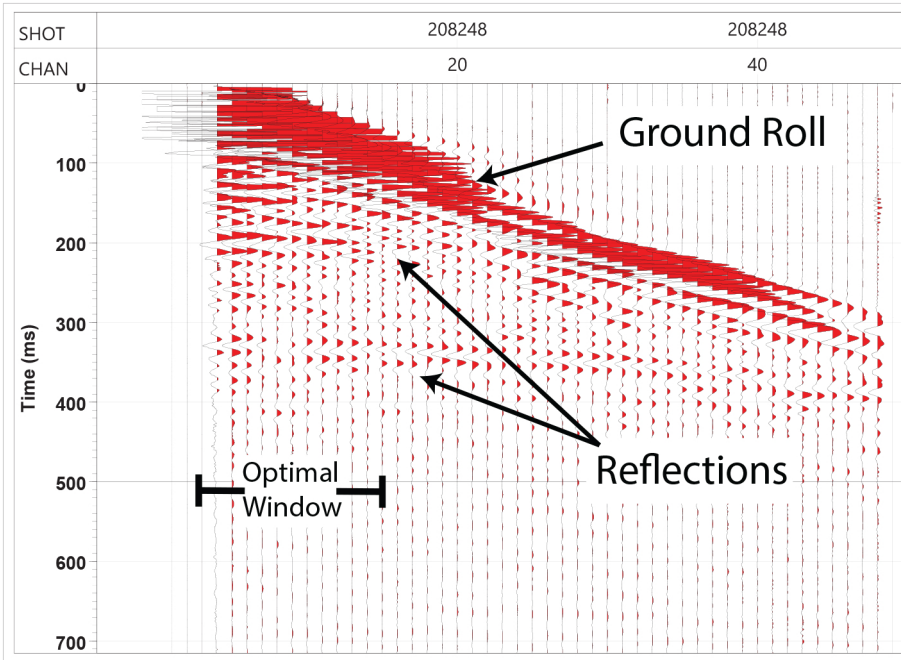

Figure 2.3: Field gather showing the optimal window for near-offset seismic reflection. The optimal window used for these data was targeting basal Quaternary reflection.

frequency, and amplitude changes that are caused by wide-angle reflections and the interaction with the free surface, SH-wave surveys must also consider the shear wave window (Harris, 1996). The optimum window should be selected so the recorded reflections are observed over the largest distance-time window possible (Hunter et al., 1984). The SH-wave surveys presented here were recorded at near-offsets of 1 m in order to target shallow intra-Quaternary reflections over the maximum distance-time window (Figure 2.3). This near-offset also limits the negative effects that are possible when recording reflections at wide-angle.

2.2 Seismic Reflection Data Acquisition

The reflection data for this work was collected on Chesshire Ln., approximately 6 km north of the Tennessee border on the active Mississippi River floodplain, in far

southwestern KY. The investigation site was selected from previous work (Woolery and Almayahi, 2014) and chosen to be coincident with the P-wave seismic lines (UK 1 and UK 1a) published by Woolery and Almayahi (2014) (Figure 1.2). This work targets the transpressional structure imaged in deeper stratigraphy by Woolery and Almayahi (2014) but investigates their potential near-surface extension within Quaternary sediments.

Our survey started 100.5 m from KY-94, with 48, Mark Products 30-Hz, geophones oriented for SH-wave collection, spaced apart at 1 m. Each of the 48 geophones were connected to a Geometrics engineering seismograph through 2, 24 takeout cables with ruggedized Mueller clips. The survey was conducted in an end-on, roll-along fashion, shooting 1 m off the first geophone, moving through 24 active geophones and then "rolling along" onto the next 24 geophones. The energy source used for all seismic data was a 1.4 kg sledgehammer, striking the flanges of an orthogonally placed steel H-pile (SH-mode). There were a series of 2 hammer strikes that were vertically stacked in reverse polarities (striking south and north) at every shot point. In order to ensure the reflection events in the recordings are SH-wave and not P- or SV- events, polarity reversals for each shot were completed and stacked in field recordings. This effectively removes non-SH-wave reflections that may interfere or bias interpretations (Woolery et al., 1993, 1996). A total of 336 total shot points were collected throughout the survey. Acquisition parameters such as recording window, sample length, etc. are included in Table 2.2.

Table 2.1: Acquisition parameters for raw field data collection.

Survey	UK-1b
Source	1.4kg hammer
Mode	SH-wave
Record Length	1.024 seconds
Sample Interval	0.125 seconds
Geophone Spacing	1 meter
Shot Spacing	1 meter
Near-offset	1 meter
Fold	6
Shots per Station	± 2

2.2.2 Seismograph and Geophones

These data were collected with a Geometrics Stratavisor NZ-series, 24-bit seismograph. SH-waves were recorded with Mark Prodcuts 30 Hz horizontally-oriented geophones. 48 geophones were connected to the seismograph through 2, 24-channel takeout cables with a spacing between each geophone of 1 m. The geophones were arranged in an end-on array with 24 out of the 48 active at a time. Each geophone was coupled to the ground with a three-inch spike and leveled with a bubble level on the top of each phone. Temporal record length for each sample was 1.024 seconds and the sampling rate used was 0.125 seconds (Table 2.2).

2.3 Seismic Reflection Data Processing

After raw data were collected in the field (Figure 2.4), processing algorithms were applied to maximize the signal-to-noise ratio (Baker, 1999). These data were processed on an AMD Ryzen Threadripper 2950x 16-core CPU home-workstation, using Schlumberger's commercial seismic-processing software, VISTA 2016.

The first step taken in processing these data was to reformat the data sets from the internal seismograph format, SEG-2, into VISTA's internal SEG-Y file format.

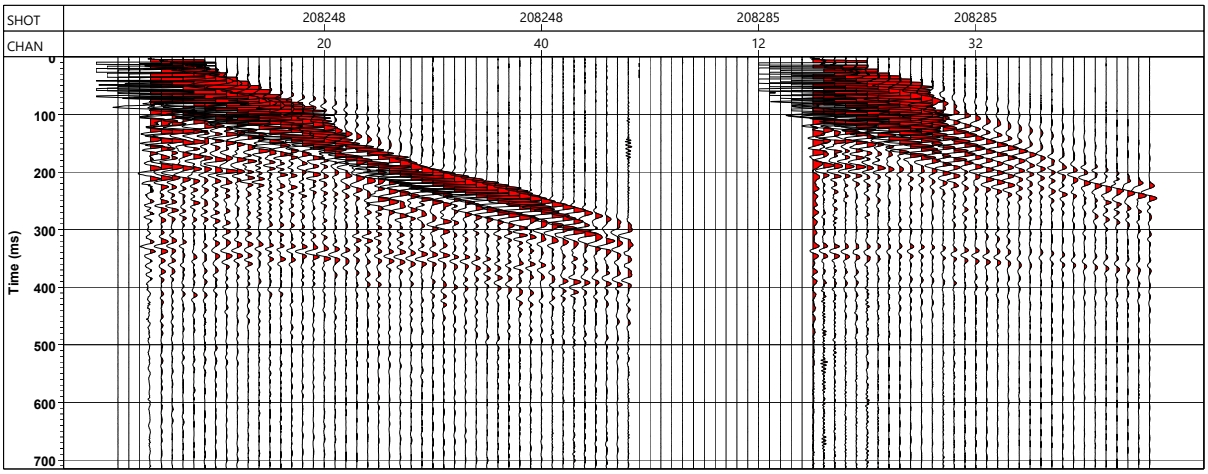

Figure 2.4: Raw field gathers from the UK-1b SH-wave survey.

The data must be reformatted before the field geometry can be written to the header files. Field geometry information defines crucial source, receiver, and surface information regarding the survey array setup. After geometry was written to the file headers, noisy traces were then deleted and coherent top muting was applied to target arrivals such as refracted waves and ground roll (i.e., Love wave for SH-mode).

The data were then scaled using a variety of scaling algorithms to continue improving the signal-to-noise ratio. Signal scaling is important because the amplitude of the signal decreases significantly with distance from the source (inversely proportionate) and higher frequencies get attenuated by subsurface material faster through attenuation and absorption of energy. Reflection signal routinely has a higher frequency content and a much lower recorded amplitude than coherent noise (Baker, 1999; Yilmaz, 2001). First a Time Variant scale was applied, which works to scale the data with the mean amplitude calculated within a defined data window (start time and end time). The value of the scalar quantity determined by: $\frac{ScaleFactor}{MeanAmplitude}$, is then posted at an "apply time". The defined time windows are outlined in Table 2.10.

This scaling algorithm finishes by multiplying each individual sample by the scalar quantity, within the data window at the given apply times. A mean scale was also applied initially to the data, which calculates a defined scale function (mean scale) and multiplies the entire trace and every sample by: $\frac{Scale}{Average}$.

Frequency bandpass filtering is a key component of seismic processing and works to increase the signal-to-noise ratio by passing the desired frequency content and rejecting signal outside of the selected bandpass (Baker, 1999; Yilmaz, 2001). In order to determine an optimal bandpass frequency range, the dominant frequencies were determined for each reflecting horizon from frequency spectrums. The dominant frequencies were determined to be 46 Hz, 51 Hz, and 54 Hz for the Quaternary gravel, coarse sands, and fine sands, respectively. A band-pass filter was then applied to the data set, with the selected filter of 20-30-70-80 Hz.

An Automatic Gain Control (AGC) was optimized and applied to the data prior to velocity analysis. AGC is a useful scaling tool when working with seismic reflection data since coherent noise arrives at different time windows compared to the optimal window for reflections (Baker, 1999). This allows for the noise to be isolated within one AGC window. AGC works by calculating an average absolute amplitude for all trace samples and then scales each time window to a normalized amplitude for all traces within that window. The integral parameter within the AGC command is the moving time window. An optimized AGC window length will increase amplitudes for low-amplitude, high frequency arrivals, while minimizing the amplitude for arrivals that have lower frequencies and high amplitudes (Yilmaz, 2001). The optimal AGC window was determined to be $\sim$150 ms. The scaled and edited data was then input into a velocity analysis flow to create three data sets for interactive velocity picking: surface velocity semblance, common velocity stacks (CVS), and offset sorts (Figure

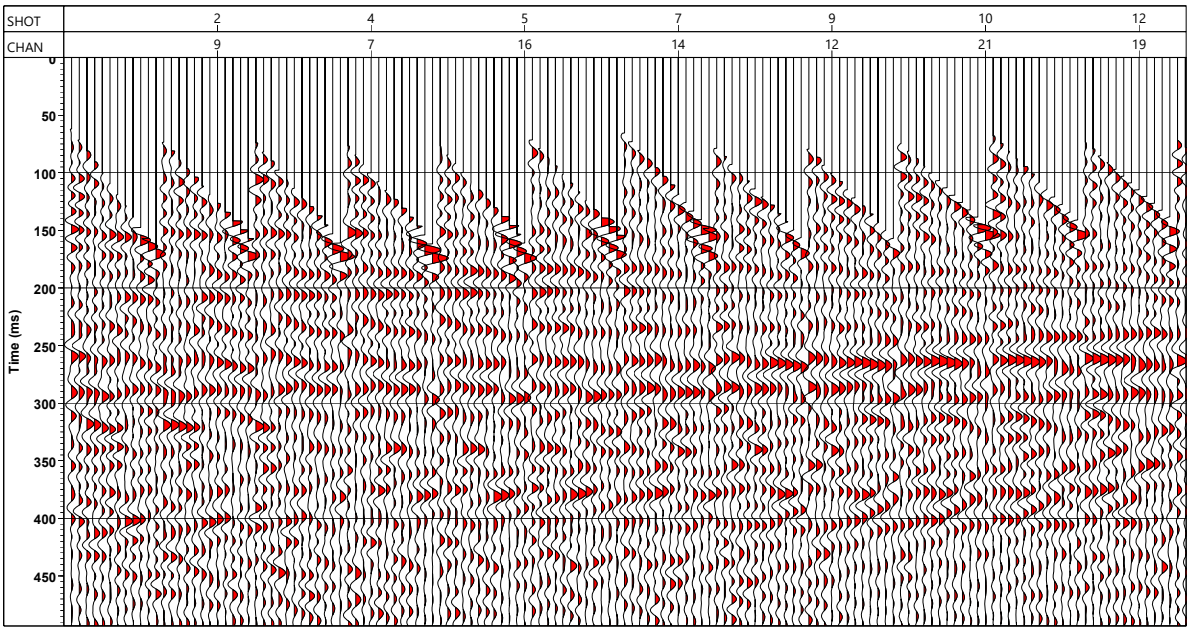

Figure 2.5: Prestacked data from UK-1b SH-wave survey. The data has noisy traces killed, a top mute applied, signal scaling and bandpass filtering.

2.6). These data sets are then synchronized within VISTA16's interactive velocity picker in order to develop a velocity model (Figure 2.7).

Normal Move Out (NMO) corrections were the next step taken in the processing routine and is required for the development of a stacked seismic image. NMO corrections work to determine the difference between a zero offset arrival and an arrival recorded as a function of shot-to-receiver distance and vertical distance from the reflection horizon (Baker, 1999; Yilmaz, 2001; Rosandich, 2019). NMO corrections are determined from the velocity model, which utilizes hand picked velocities from VISTA 2016's interactive velocity analysis (Figure 2.7). Any variance of the velocity model from the true seismic velocity of the subsurface will result in morphing of flat reflectors; either arcing the reflectors up if selected velocities are too high, ultimately correcting the NMO too much; or leaving reflections in their parabolic shape if the

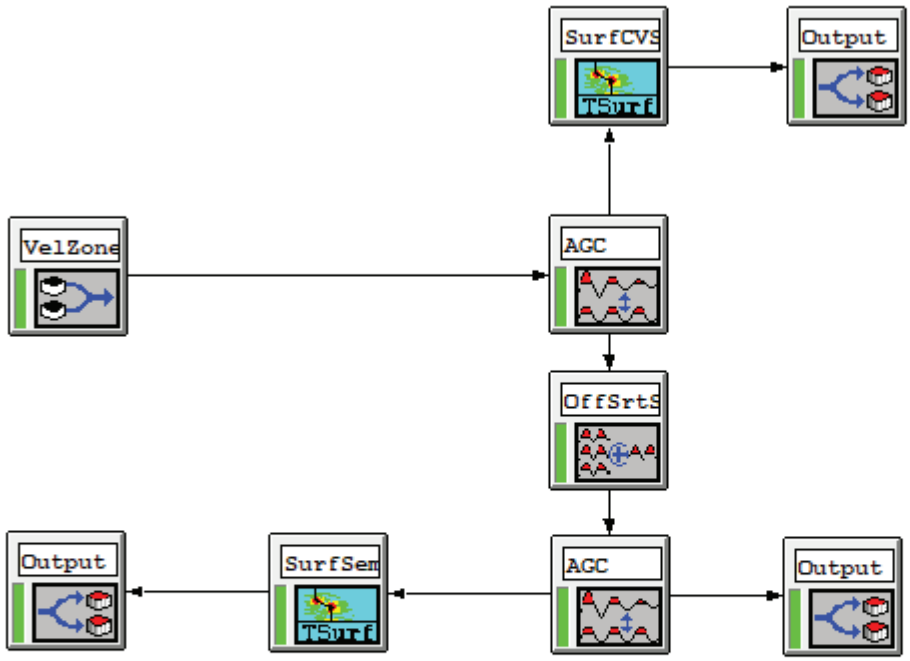

Figure 2.6: Flow used in VISTA2016 to create three data sets for interactive velocity picking. Flow generates three outputs: common velocity stacks, surface velocity semblance, and offset sorts.

correction was not enough. A NMO stretch mute was applied to the data through the velocity command through the selection of a percentage and sample range to move signal that has a velocity different from those picked, up to the picked velocity (Table 2.3). This gets rid of a significant amount of noise between strong reflectors and prevents arrivals that have been extremely distorted by the NMO corrections from being stacked (Baker, 1999). The stretch mute length utilized on these data was ~25% with an 8-sample range. The velocity model was then output from the interactive velocity selection process and smoothed to avoid any stretching of the signal due to sharp variance in velocity (Yilmaz, 2001). The scaled and edited data had NMO corrections applied and produced NMO'ed records which display flat reflections, as if

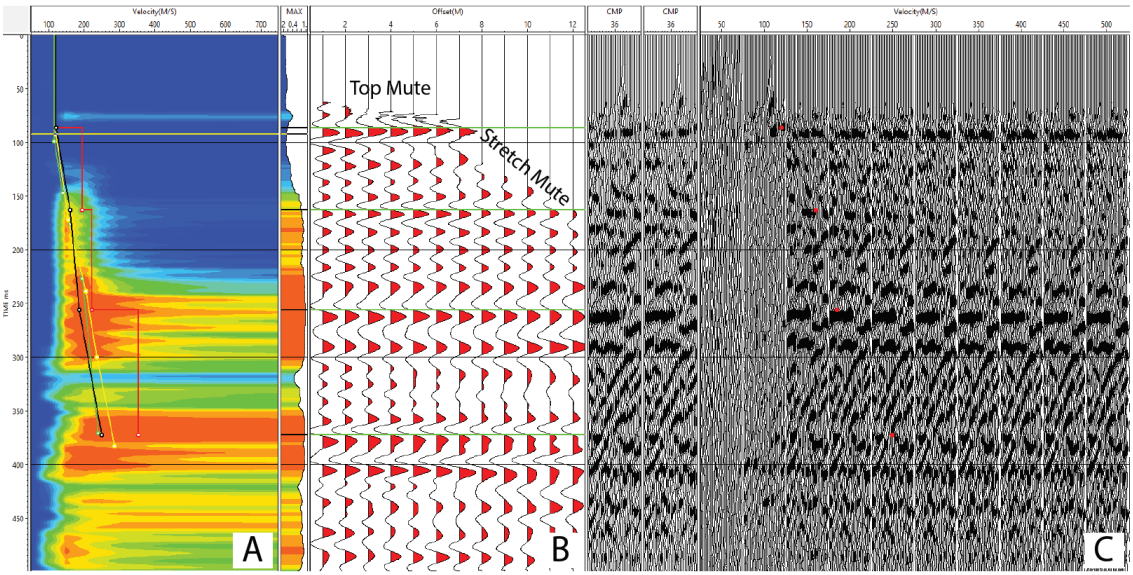

Figure 2.7: Example velocity analysis panel from VISTA16 for UK-1b SH-wave data set. A)semblance velocity B)offset gather C)common velocity stacks (CVS).

recorded using zero-offset time (Figure 2.8).

Residual statics was applied to the data prior to stacking, utilizing a power stack command. Residual statics is useful because it corrects any differentiation of travel time arrival for traces within a singular reflection, moving the reflection signal trace by trace according to a user-defined amount of time. Ultimately, residual statics improves coherency of the reflectors which increases the signal-to-noise ratio further. Elevation statics was not applied to this data as it was deemed unnecessary due to the topography change across the survey being <1 m. After the velocity model was determined and statics was applied, these data were stacked using a common mid-point (CMP) stacking method. Within the VISTA 2016 flow to stack, an output of NMO'ed records occurred right before the CMP stack command (Figure 2.9), which allowed for the NMO'ed records to be qualitatively inspected alongside a brute stack. Qualitative inspection of the NMO corrected data is a useful way to check correctness in the velocity model. These data had some additional trace balancing and filtering

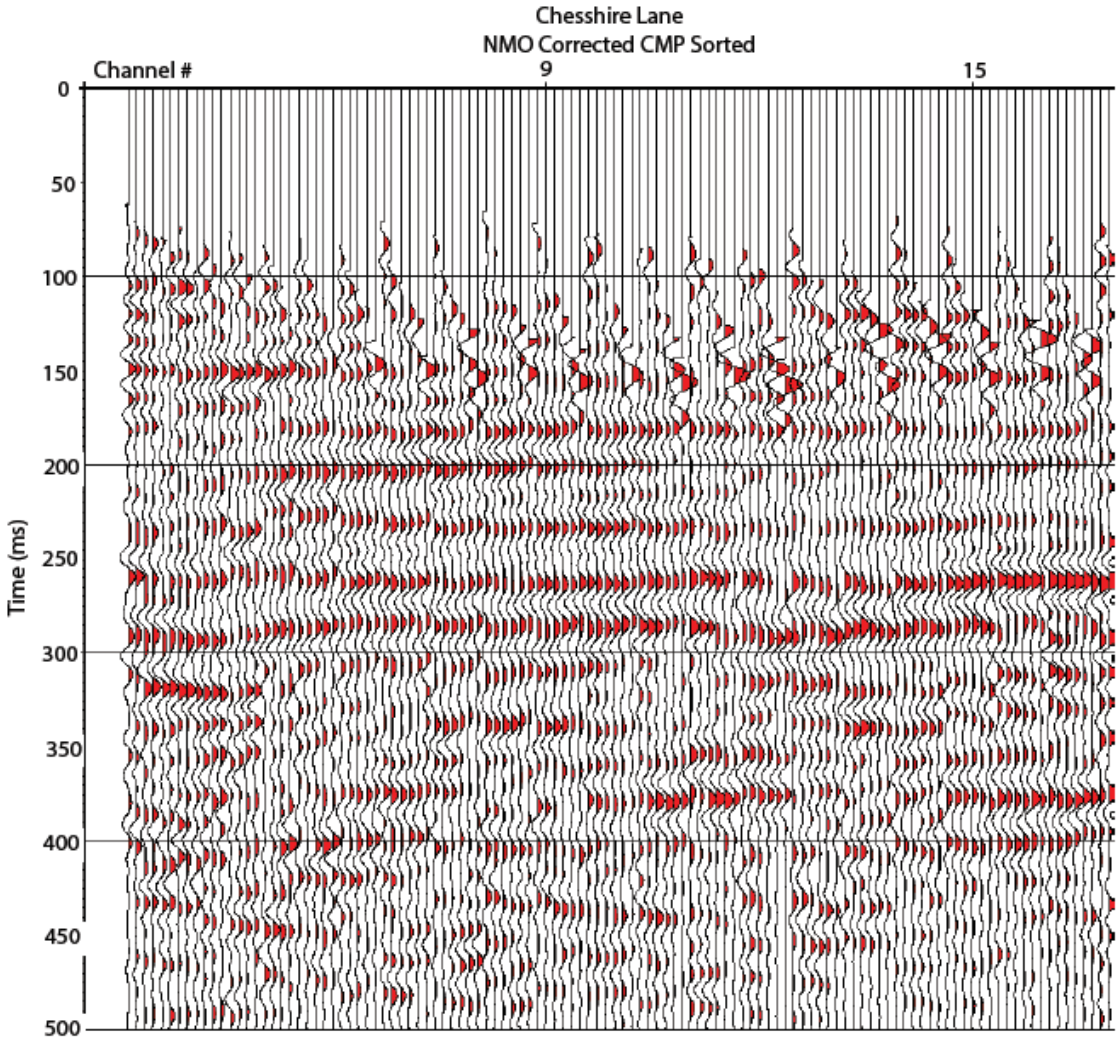

Figure 2.8: Example of NMO-corrected data from UK-1b SH-wave data. Coherent reflections have been flattened to a zero-offset time based on the velocity model produced from VISTA16's interactive velocity analysis.

applied to ensure only the desired signal was being stacked.

A FK filter was applied to the data post-stack to further reduce noise and improve coherency across reflectors. The FK filter works be transforming the data into a frequency and wavenumber domain and allows coherent noise to be rejected, thus improving the overall coherency of signal. A broad rejection filter, symmetrical about the zeroth wavenumber (Baker, 1999), was designed to target consistent diffraction

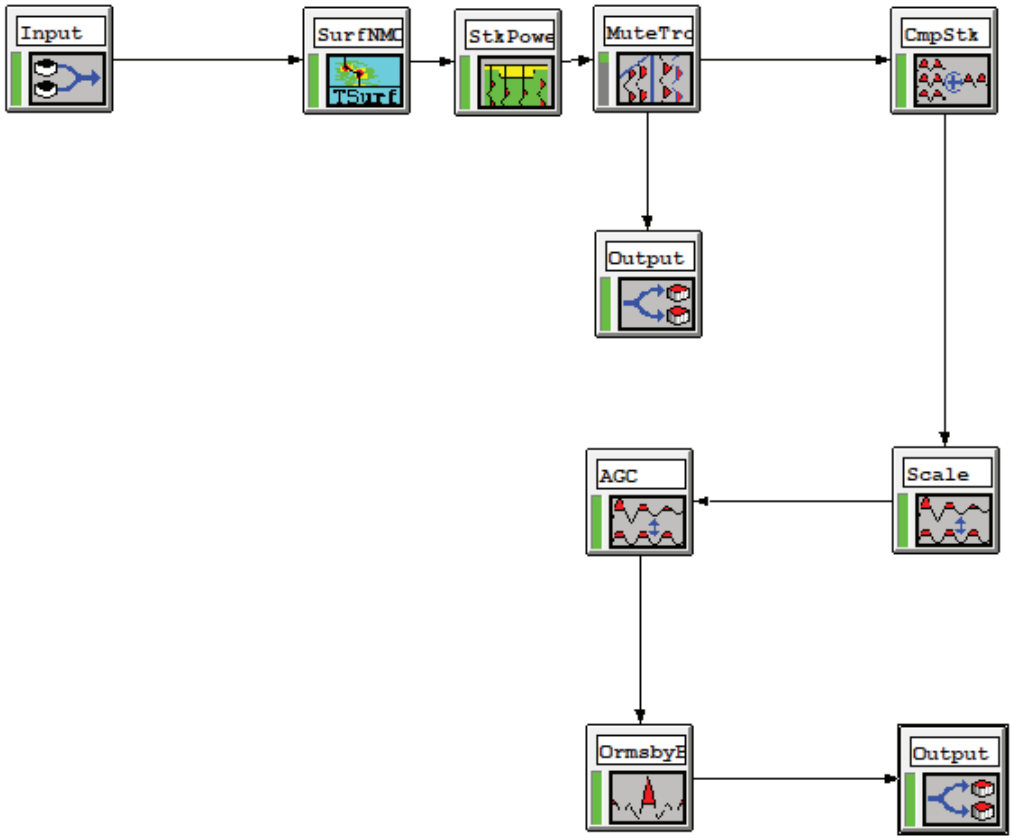

Figure 2.9: Flow executed in VISTA2016 to create a time stacked profile of the Chesshire Lane SH-wave data.

patterns that consumed the data (Figure 2.10). A variety of FK filter shapes were tested, and the selected filter was a large polygon shape (Figure 2.10). This filter did the best job of ridding the data of diffraction artifacts that contained frequency content similar to the reflection events.

After the stack flow was executed, the NMO corrected data and a stacked time section were qualitatively analyzed for high signal-to-noise ratio. This time stack was input to a flow that executed a time-to-depth conversion based on the velocity model.

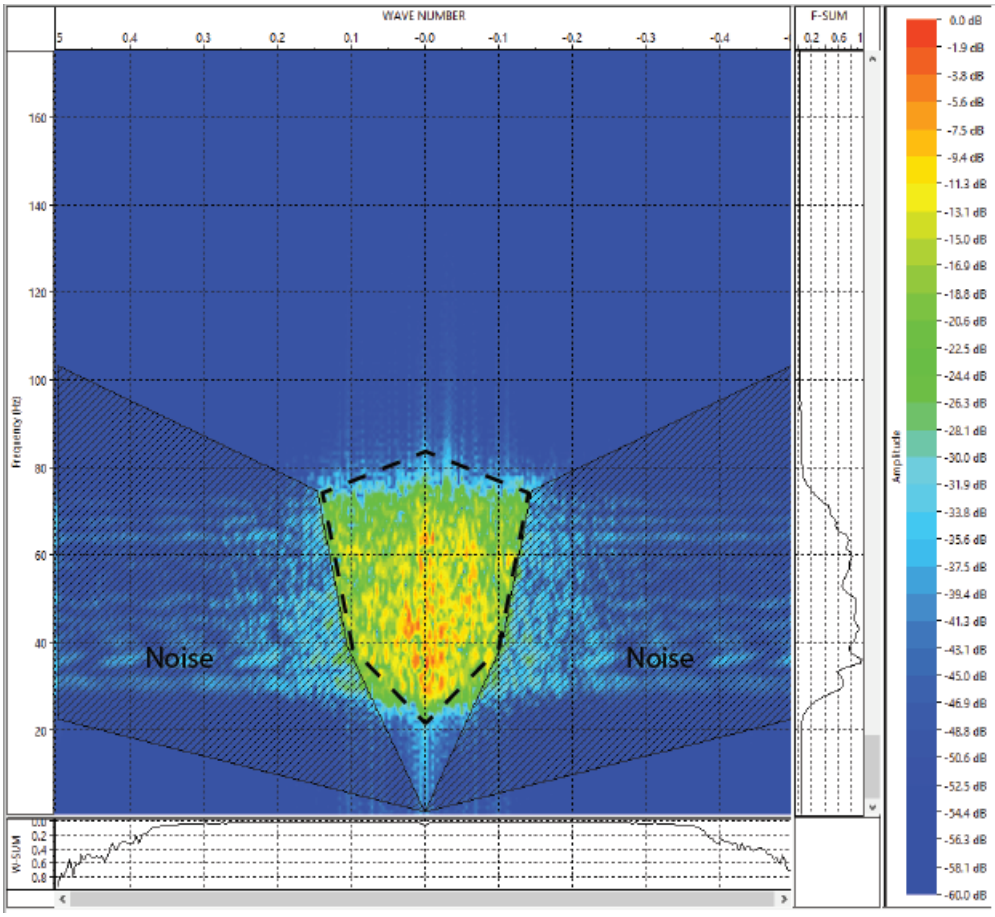

Figure 2.10: Example of the F-K filter applied to the data after the stacking process. The black dashed polygon contains the core reflection for the data set.

The depth conversion allows for stratigraphic correlation and was compared with the near-field borehole logs (CUSSO) to confirm accuracy of reflection events.

2.4 LiDAR Analysis

LiDAR analysis was conducted on the Kentucky Commonwealth database of statewide LiDAR data, in the Digital Earth Analysis Lab (DEAL) at the Kentucky Geological Survey (KGS). LiDAR point data is collected by sending hundreds of thousands of laser impulses per second from an aircraft with known altitude, GPS location and pulse orientation. The impulse returns are recorded as a point-cloud, and the position

Table 2.2: Processing sequence and parameters for UK-1b SH-wave dataset.

Processing Step	**Processing Parameters**
Reformat	SEG-2 to SEG-Y format
Geometry	Geometry definition to headers
Trace Kill	Noisy traces killed
Trace Mute	Top mute Tapered by 4 samples
Time-Variant Scaling	Start:End:Apply 0:100:50 50:150:100 100:300:200 200:400:300 300:500:400
Data Scaling	Mean scale Scale factor: 1
Ormsby Bandpass Filter	20/30/70/80 Hz Domain: Frequency Restore Mutes after Filtering
AGC	150 ms window Skip initial hard-zero
NMO Correction	Velocity Model File Percent Velocity: 100% Stretch Mute: 25% Mute taper: 8 samples Scan from top for stretch mute
Stack	Stack: No Normalization Stack Common Mid-point Stack
F-K filter	F-K designed filter file Power amplitude: 1 Smooth traces: 7 Smooth frequency: 5 F-K operation: Reject
Depth Conversion	Time to depth conversion from input velocity file Increment: 0.1 End: 250

of the surface is calculated from the two-way travel time of each returning laser pulse and their phase differences. This point cloud is then classified manually to identify a ground surface, which is interpolated into a digital elevation model (DEM) available from KGS.

To create a series of roughness maps mean, maximum and minimum DEMs were generated at a variety of smoothing window sizes (Table 2.3). Rectangular smoothing windows create significant artifacts as artificial boundaries from raster data and tiles are typically enhanced. Thus, a circular smoothing window was used as it produced the fewest artifacts. Smoothing window sizes varied from small cell radii (n = 10 meter or 7 cell diameter) to large radii (n = 901 meter or 601 cell diameter) to ensure different size surface features, specifically those across Sassafras Ridge, are adequately captured. Raster calculator was used to generate a roughness map for each window size. The overall process follows equation 2.2:

$$Roughness = \frac{W_s(mean(DEM)) - W_s(min(DEM))}{W_s(max(DEM)) - W_s(min(DEM))} \tag{2.2}$$

where W_s is window size and DEM is a smoothed 10ft digital elevation model. Surface roughness is an important land-surface parameter used to identify individual landforms and the processes acting upon them (Frankel and Dolan, 2007; Grohmann et al., 2010). Each of the roughness maps were then converted to ASCII files and imported into MATLAB for analysis using a hyperscale script written by Dr. Jason Dortch of the KGS. The hyperscale script vertically stacks roughness maps, layering them on top of each other, and undertakes vertical column analysis through all window sizes to generate two maps. The first map generated is a maximum value map (Figure 2.11), which records the maximum roughness value for each column of pixels across all smoothing window sizes. This shows how well each column within the map

was captured by our selected window sizes. Topography that resonates perfectly with a given wavelength or window size will return a value of one, while topographic raster cells that are not captured by a given wavelength (i.e. flat) will return a zero value. The goal of the max value map is to ensure that the stacked smoothing window sizes adequately capture surface features. We defined adequately as the majority of the surface displaying values of > 0.5. The second map generated from the MATLAB script is an index map of maximum roughness values (Figure 2.12, which shows the layer corresponding to the maximum value stacked roughness maps. This index or hyperscale map shows which swaths of landscape are best represented by a particular window size. Thus, interrogating a land form on a hyperscale map will identify which scale(s) best isolate features of interest. Hyperscale analysis of roughness maps have proven useful in distinguishing boundaries between geomorphic landforms (Lindsay and Newman, 2018).

The smoothing window sizes ranged from a 3-300 cells (radius) across 14 different window sizes with 35-150 cell radius highlighting most area corresponding to surface feature along Sassafras Ridge (Figure 3.6). The 35-cell radius window size was selected for mapping due to the least presence of artifacts and ringing from man-made structures in the area, such as roads and train tracks. Both the 35-cell roughness map and a hill shade of the roughness map was used for mapping terrace sequences in the greater Sassafras Ridge area (Figure 3.7).

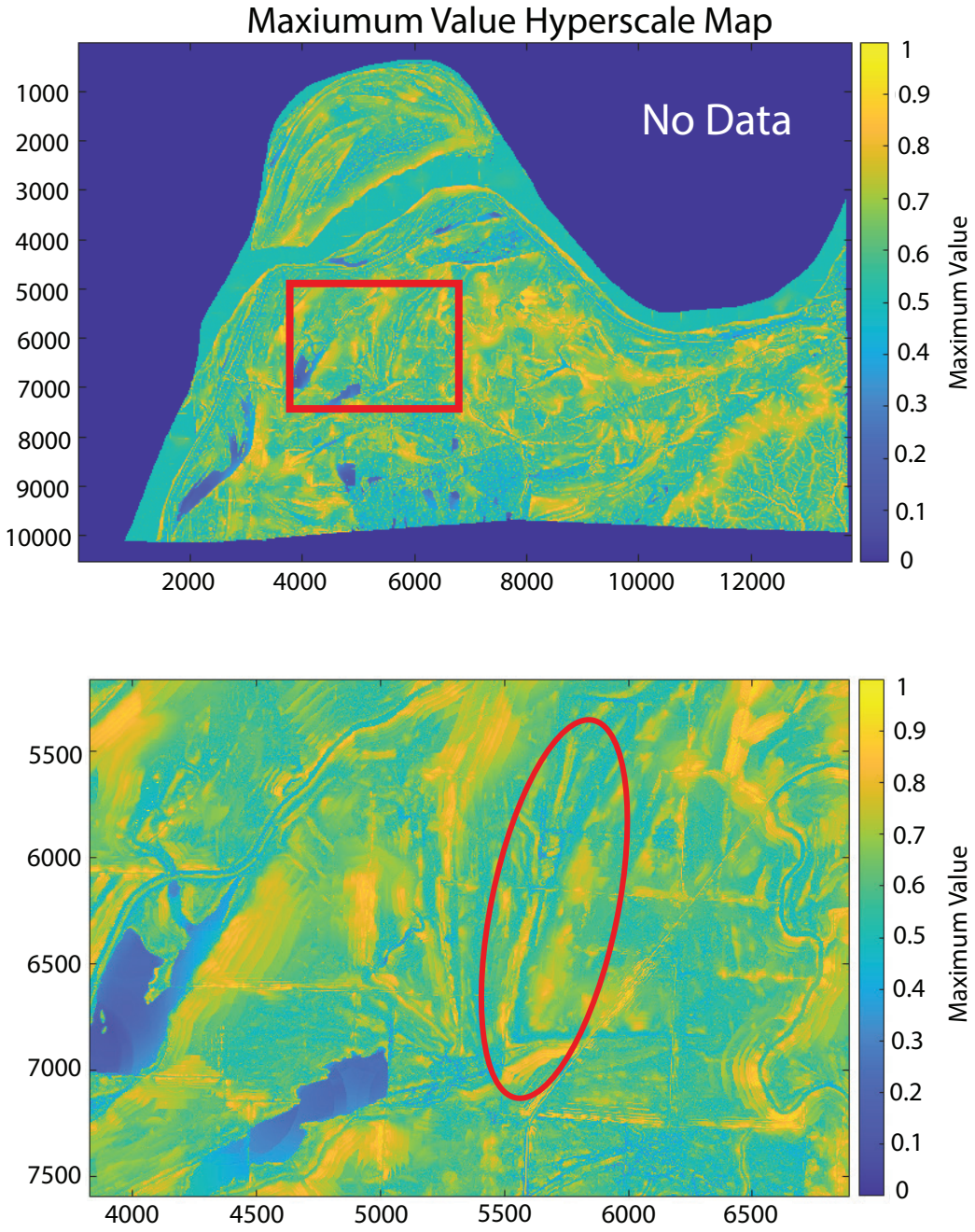

Figure 2.11: Maximum value hyperscale map generated from Dr. Jason Dorth's hyperscale script. Depicts the highest roughness value for each column of pixels across all smoothing window sizes. Adequately captured topographic detail should return a maximum value of > 0.5.

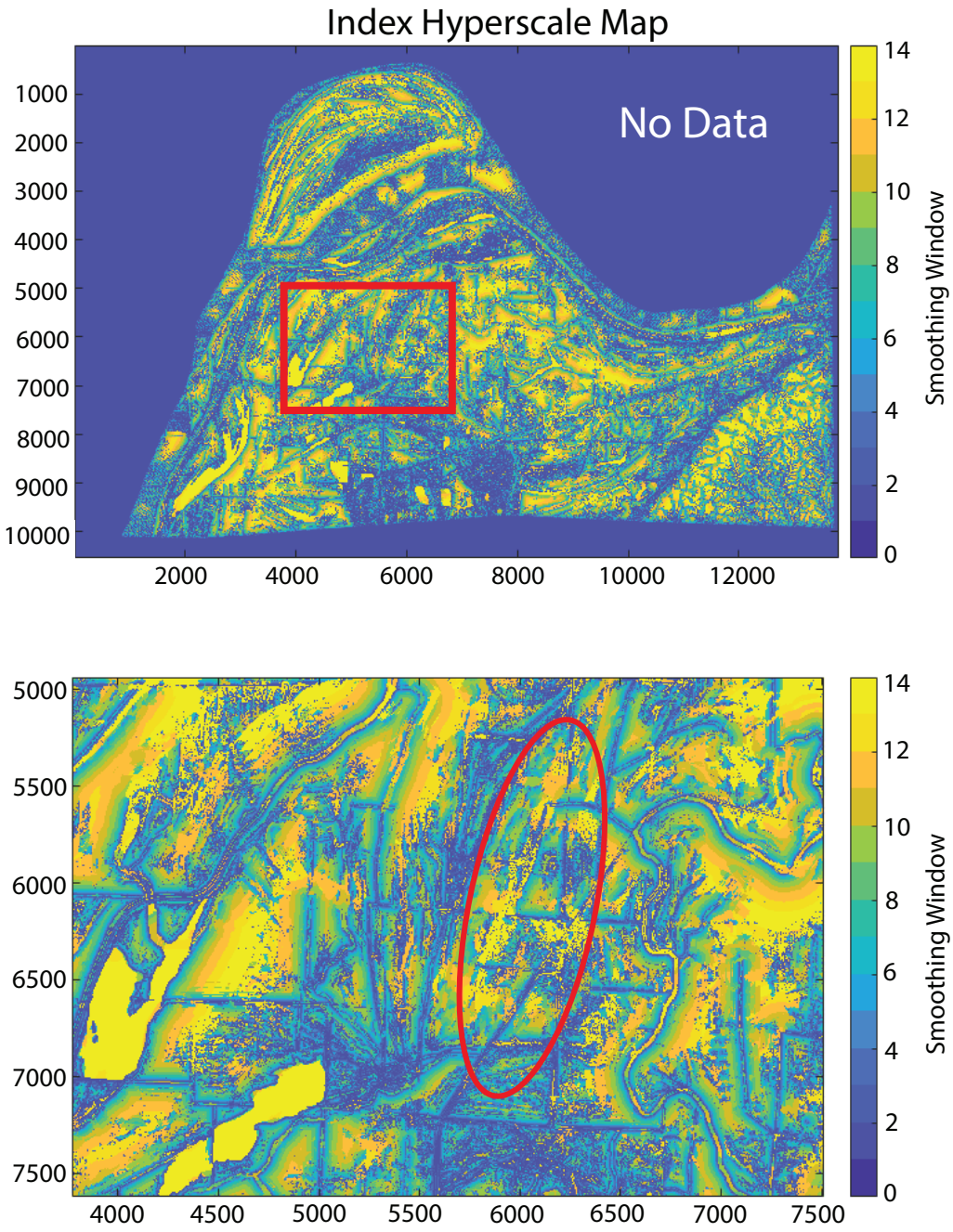

Figure 2.12: Index map generated from the hyperscale script. Each color corresponds to the stacked layer that returned the highest maximum value. There were 14 smoothing window sizes used and are outlined in Table 2.3.

Table 2.3: Smoothing window size parameters utilized in the hyperscale roughness map. The bolded window sizes show corresponding wavelength with the most area of Sassafras Ridge (35-150).

Radius (cells)	Diameter (cells)	Diameter (meters)
3	7	10
7	15	22.5
10	21	31.5
15	31	46.5
20	41	61.5
25	51	76.5
35	**71**	**106.5**
50	**101**	**151.5**
75	**151**	**226.5**
100	**201**	**301.5**
150	**301**	**451.5**
200	401	601.5
250	501	751.5
300	601	901.5

Chapter 3 Results

3.1 UK-1b SH-wave Seismic Line

The UK-1b line is a 6-fold, 682 trace profile, which represents approximately 340 meters of total subsurface coverage (Figure 3.4). These data were acquired 12 km northeast of the Reelfoot scarp, coincident with traces 175 to 325 of the P-wave data in Woolery and Almayahi (2014) (Figure 1.2). The profile focuses on shallow subsurface coverage, <50m, across the main transpressional feature interpreted from Woolery and Almayahi (2014) profile UK-1a. The data quality of UK-1b is good, but has numerous diffraction patterns associated with the boundary discontinuities; a common artifact associated with faulted zones. Although migration and other means of mitigating diffractions were not applied, the correlation between the diffraction patterns and the interpreted deformation suggests the diffractions are related to the deformed sediments within the fault zone. A significant percentage of the diffraction patterns were successfully filtered with a post-stack FK filter but some remain due to discontinuities and degree of faulting that occurs within the near-surface (Figure 3.1).

Stratigraphic correlation was done on the high-quality data using the adjacent CUSSO borehole logs as a control. We observe large amplitude and coherent reflection events that occur between 250 – 330ms, 150-200ms, and 80-110ms (Figure 3.2). These reflectors were interpreted to be the top of the basal Quaternary gravel (Unit 1), the top of the red/blue coarse sand (Unit 2), and the top of the fine brown sand (Unit 3), respectively (Table 1.1). There are defined areas where the reflectors lose coherency, commonly due to transpressional faulting causing through deformation degradation of the sharp impedance contrast (Dix, 1955). Interpretations of faulting are based on abrupt dip changes, vertical offset between reflectors, and coherency loss

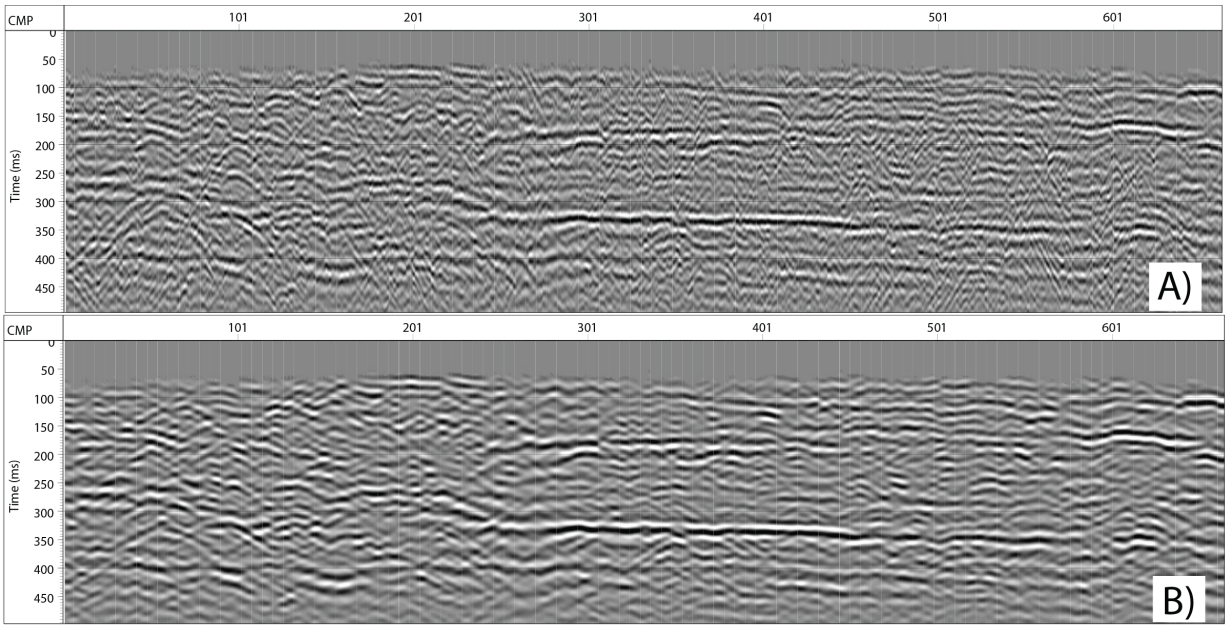

Figure 3.1: Results of the FK-filter. A) shows a time profile for the UK-1b SH-wave data set prior to FK-filter application. B) shows the same time profile with the designed rejection FK-filter from Figure 2.10 applied post-stack.

Table 3.1: Vertical resolution and detectable limit for the UK-1b SH-wave data set.

Reflection Event	Dominant Frequency (Hz)	Dominant Wavelength λ (m)	Vertical Resolution (m)	Detectable Resolution (m)
Top of Fine Sands	54	2.6	0.65	0.3
Top of Coarse Sands	51	3.2	0.8	0.4
Top of Quaternary Gravel	49	4.3	1.1	0.6

of reflection events in the profile. We calculated both the vertical resolution ($\lambda/4$) and the Widess resolution ($\lambda/8$) Widess (1973) at each reflector; with calculated resolutions determined to be 1.1 m at the top of the Quaternary gravel, 0.8 m at the top of the coarse red and blue sands, and 0.65 m at the top of the fine brown sand (Table 3.1) (Widess, 1973; Yilmaz, 2001). The vertical resolution limit determined for each reflection horizon is smaller than the vertical offset observed across each reflector, supporting the interpretations that the measured vertical offset is real.

Offset and warped reflectors, areas of varying coherency, dip change across reflectors, and extensive diffraction patterns are observed throughout the record and as shallow as the array aperture was able to image (<10m). The largest area of deformation lies between CMPs 140-240; a 100m wide area of coherency loss and diffraction patterns bounded on both edges by coherent but offset reflectors (Figure 3.4). The total displacement for each reflecting horizon was determined by taking depth measurements from the undisturbed reflectors adjacent to the deformed zone. This zone of deformation has vertical displacement of at least 9m at the top of the Quaternary gravel accommodated by transpressional faulting. There is additionally at least 4m of offset across the unit 2-3 interface, indicating vertical displacement resulting from faulting within 10m of the surface. There are three interpreted faults within the eastern deformation zone (A, B, and C), with each fault cross-cutting the basal Quaternary reflector and continuing into the late-Quaternary sediments (Figure 3.4). Between the individual faults reflectors have been disrupted and warped, forming anticlines between each fault (e.g. traces 50-250). The faults interpreted within this zone of deformation are near vertical and correlates with the "flower structure" in the deeper strata interpretations of Woolery and Almayahi (2014) (Figure 1.2). The spatial and architectural style of these faults are also consistent with the Pratt (2012) hypothesized through-going shear zone, showing N30E strike and dextral offset. The fault zone is within the northwestern margin of the hypothesized shear zone by Pratt (2012) and shares consistencies with the transpressional structure presented by Rosandich (2019), also within the bounds of the hypothesized shear zone, 12 km to the southwest.

Fault A is located at trace 50 and defines the eastern margin of the largest zone of deformation. This fault was interpreted based upon reflection coherency loss across the three unit horizons and dip changes across the reflectors. Diffraction patterns assisted

with the placement of the fault in the profile, as they are characteristic of discontinuities (i.e. a fault plane). Fault A is near-vertical representing part of the near-surface expression of the transpressional structure imaged in deeper stratigraphy by Woolery and Almayahi (2014). Fault C is located at trace 250 and defines the western margin of the eastern zone of deformation (Figure 3.4). This fault was also interpreted based on reflector coherency loss and horizon dip reversal moving through the zone of deformation. Fault C is also a near-surface expression of the deeper transpressional structure, extending to less than 10 m of the surface. Fault C is near vertical, forming a graben structure with fault A. C also shows west-side displacement of the Quaternary Gravel and late-Quaternary sediments. Fault B is a fault interpreted in the middle of the eastern zone of deformation, showing near-vertical trend, dip changes, and offset across reflectors. Antiformal features are observed between this fault and faults A and C. The antiforms vary in structural amplitude and qualitatively appear to have varying offset across the width of the deformation zone.

There is a second zone of deformation at the western end of UK-1b, between CMPs 560 and 660, recognized as a 50 m wide area of amplitude changes, coherency loss, anticlines and strong diffraction patterns (Figure 3.4). This area is bounded by coherent, strong reflectors to the east and warped and offset reflectors to the west. Amplitude change, coherency loss, and vertical displacement is observed across each reflector, as shallow as 5 m. The vertical displacement is approximately 4 m across unit 1-2 and unit 2-3 interface, measured across the coherent reflectors on each edge of the deformed zone. Two faults are interpreted in this area (faults D and E) and are near vertical faults defining the margins of this deformation area. Faults D and E form a smaller graben similar to faults A and C, characteristic of transpressional "flower structures". Fault D marks the eastern margin of the zone and extends to $\sim$8 m below ground surface. This fault offsets the western edge of a paleochannel feature

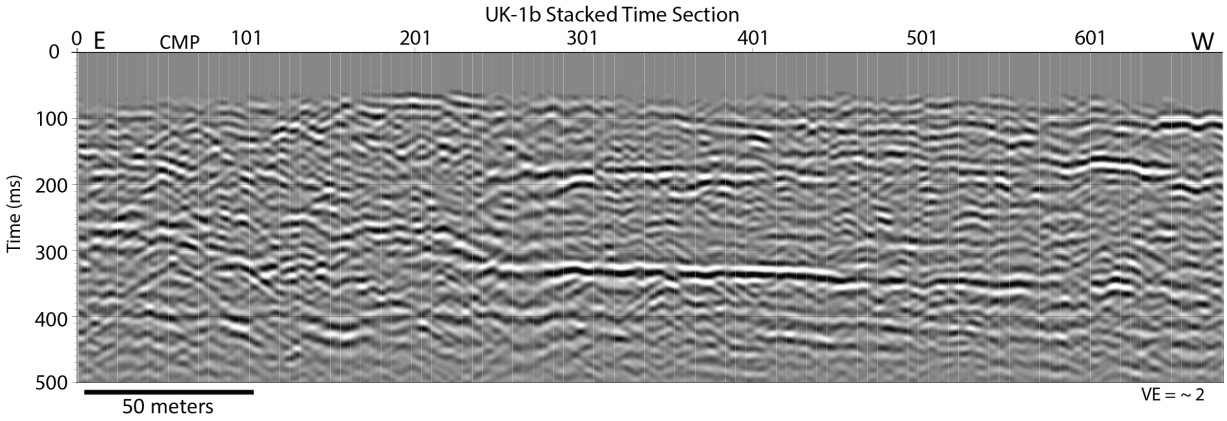

Figure 3.2: Un-interpreted UK-1b SH-wave stacked time profile. Reflections occur at 250-330ms, 150-200ms, 80-110ms and are interpreted to be the top of the Quaternary basal gravel, the top of the Quaternary red, blue coarse sands and the top of the Quaternary fine brown sand units, respectively.

located at the top of unit 3. Fault E marks the western margin of the smaller zone of deformation and offsets unit 2-3 interface approximately 4 m, but seems to terminate before reaching the top of unit 3, at ∼10m depth. There is another possible fault within the zone but was not clearly defined due to degree of deformation.

There is a noticeable "hinge" feature along the top of the basal Quaternary gravel (Unit 1), where the reflector changes from westerly dipping to easterly dipping around CMP 500. A possible fault has been interpreted here but does not affect the unit 2-3 interface, so it is likely that the fault terminates within unit 2. Unit 2 exhibits sediment thickening towards the west, characteristic of syndepositional faulting and reactivation during Quaternary deposition (Figure 3.4).

3.2 LiDAR

Spatial and relative temporal characteristics of the surficial features around Sassafras Ridge were defined using a LiDAR derived DEM, slope angle map, and roughness maps (Figure 3.5, 3.6 and 3.7). The terrain ranges in elevation from undisturbed

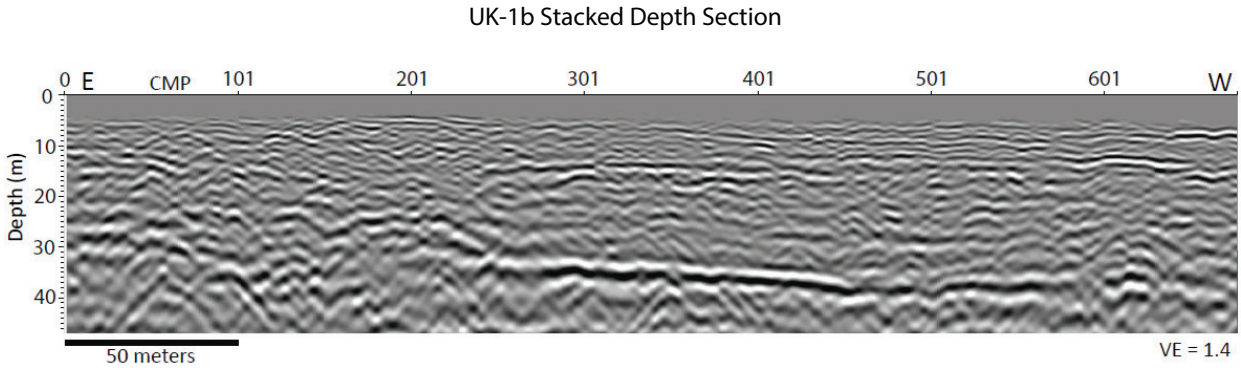

Figure 3.3: Un-interpreted UK-1b SH-wave stacked depth profile. Reflections are based on their depth at CMP 301 due to the vertical offset across the profile. Reflections occur at 35m, 15m, and 7m and are interpreted to be the Quaternary basal gravel, the top of the Quaternary red, blue coarse sands and the top of the Quaternary fine brown sand units, respectively.

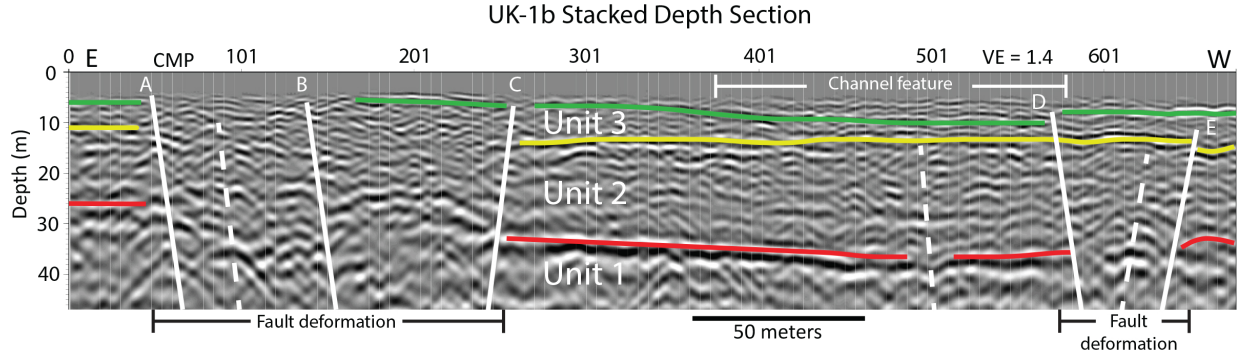

Figure 3.4: Interpreted UK-1b SH-wave stacked depth profile. Reflections are based on their depth at CMP 301 due to the vertical offset within the profile. Reflections occur at 35m, 15m, and 7m and are interpreted to be the Quaternary basal gravel, the top of the Quaternary red, blue coarse sands and the top of the Quaternary fine brown sand units, respectively. Channel feature identified between CMPs 380-580 in the upper 8m of the subsurface. Areas of fault deformation are marked between the black brackets.

dendritic drainage, to a series of arcuit surface features interpreted as atleast eleven (A-K) flights of terrace packages, down to contemporary Mississippi River, which sets base level (Figure 3.7). The terrace packages were differentiated from tectonic surface expressions due to the arcuit nature of each terrace, compared to a linear tectonic expression. Cross-cutting relationships show that each terrace package comprises individual terraces with a unique orientation and curvature we hence forth refer to as terrace grain. Initial mapping of the terrace packages in the greater Sassafras Ridge area allows us to determine a relative sense of timing between each package, as well as as cross-cutting linear tectonic expressions. Mapping differential terrace grain helped further to differentiate terrace packages and determine a timing of deposition versus tectonic deformation across the Sassafras Ridge lineament.

Interrogation of the 35 cell roughness map (Figure 3.6) revealed a 100m wide zone of strike-slip deformation on the eastern side of the UK-1b line that is coincident with the lineament feature, confined by roughness hill shade (Figure 3.7). The nose-shaped steep slopes bounding Sassafras Ridge clearly demarcated in Figure 3.5, conclusively outlines terrace package boundaries where paleochannel erosion and deposition direction dramatically changed. Thus, the possibility of the entire Sassafras Ridge being a pressure ridge is precluded. In contrast, the lineament, and subtle pressure ridges on both sides, clearly cross the terrace grain (Figure 3.7) demonstrating that deformation is post-Sassafras terrace deposition and younger than terrace package C (Figure 3.5 and 3.7). It is likely that with the degree of deformation imaged in the subsurface and the spatial location that the lineament is an expression of surface exposure of the strike-slip faults.

We assume that all terrace packages were developed within the Quaternary and are related to meandering of the Mississippi River after the destruction of the Teys and

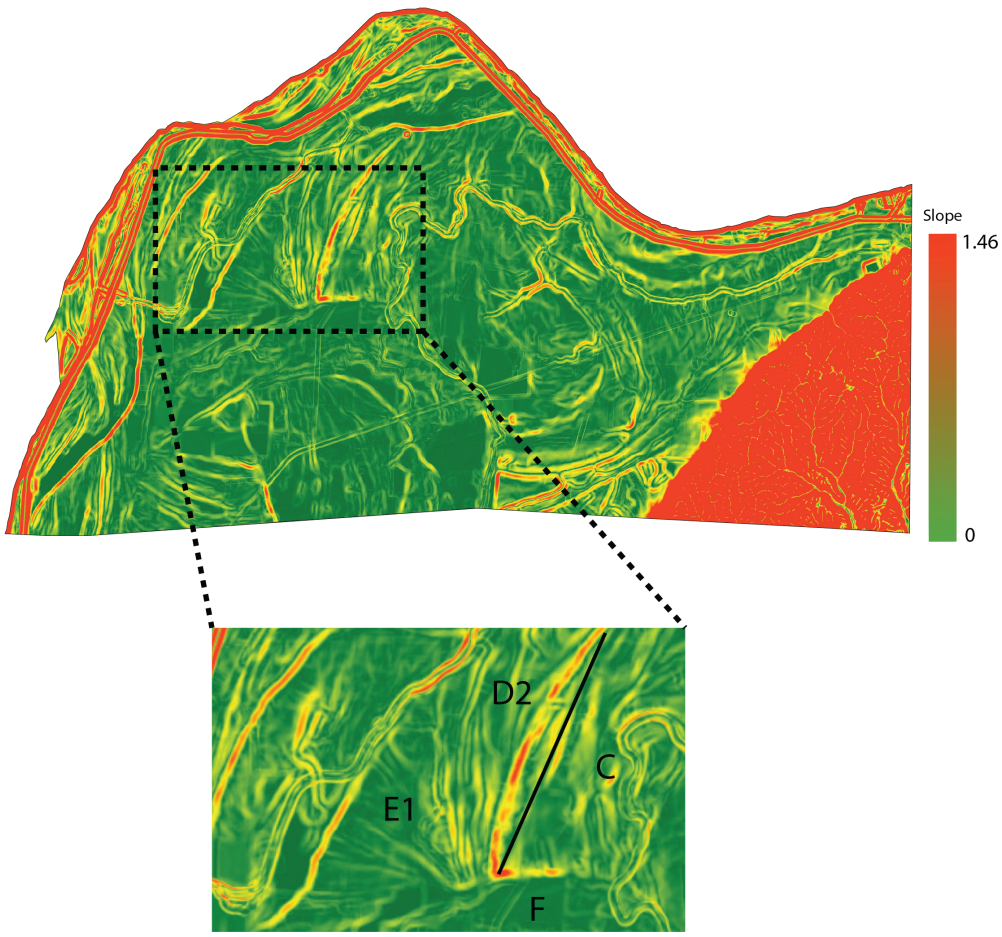

Figure 3.5: Slope map of southwest Kentucky, with the black dashed box outlining the greater Sassafras Ridge area, with a 35-cell smoothing window applied. The solid black line defines the lineament under investigation. Labels C, D2, E1, and F shows spatial locations of differing terrace packages bounding the lineament.

development of the Ohio tributary. Thus, surface lineament features occurred after the deposition of terrace package C and can be categorized within the Quaternary time. Terrace package D2 is the next deposit temporally to come through the area and bounds the western edge of package C. Terrace package E1 bounds package D2 to the west and shows an alluvial fan style deposit. The southern boundary of these terrace packages (C, D2, and E1), as well as the lineament under investigation get truncated by what appears to be a paleoriver channel that fed into the Mississippi (terrace package F) (Figure 3.7).

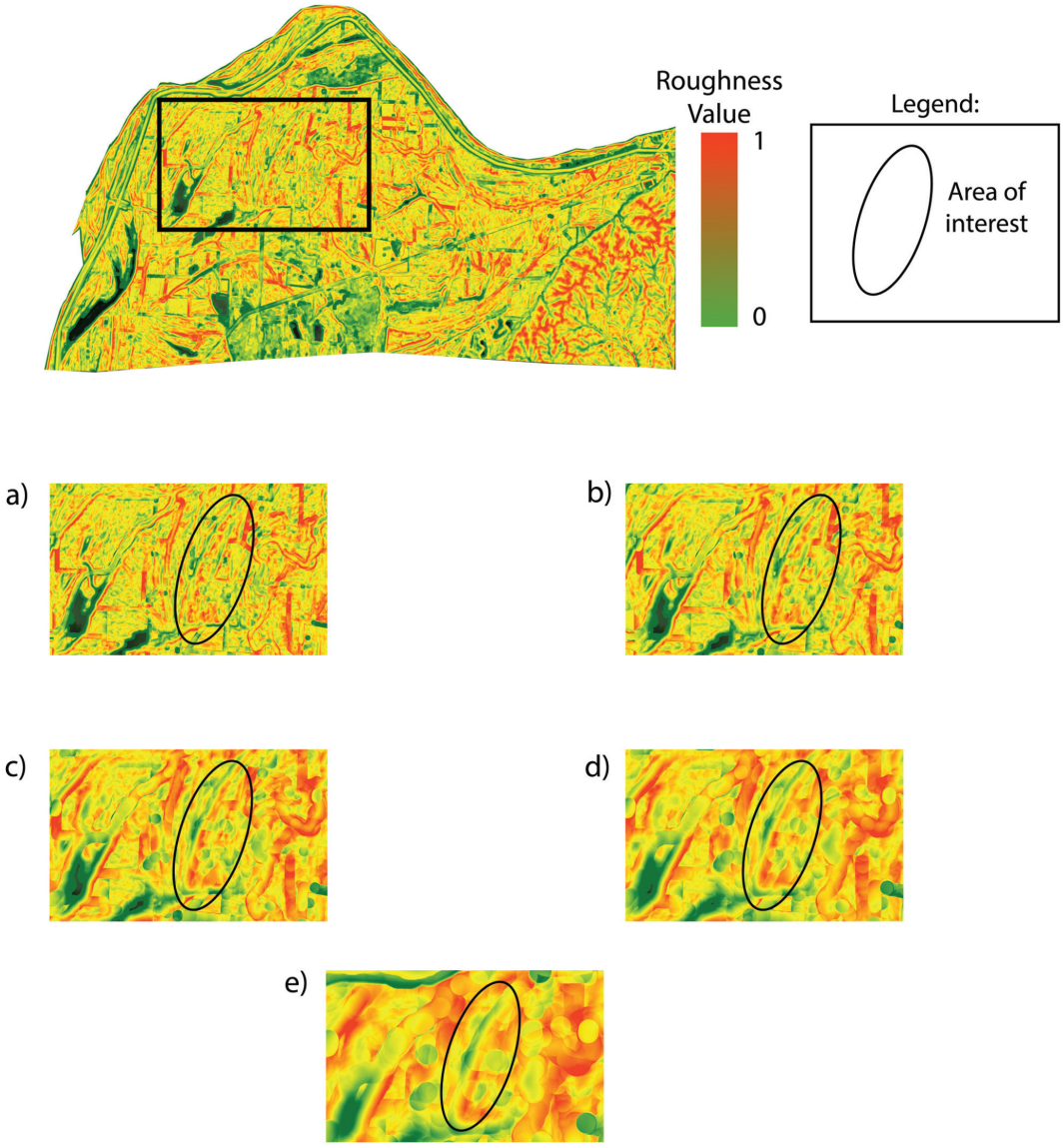

Figure 3.6: Roughness map with a 35-cell smoothing window with the area outlined by the black box showing the area of interest: Sassafras Ridge. A) shows 35-cell smoothing window. B) is 50-cell smoothing window. C) is 75-cell smoothing window. D) is 100-cell smoothing window. E) is 150-cell smoothing window. These window sizes were determined from the hyperscale maps (Figure 2.11 and 2.12) as highlighting the most area along Sassafras Ridge.

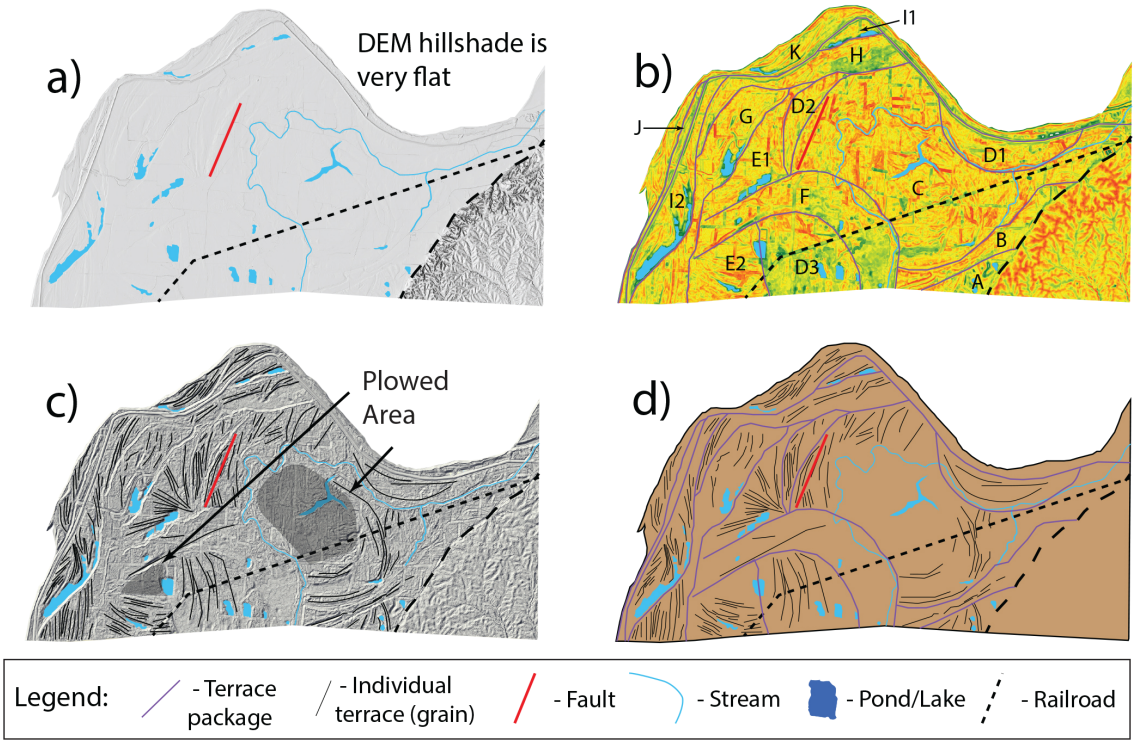

Figure 3.7: Maps showing the area northeast of the Reelfoot Fault of NMSZ, previously depicted by the red box in Figure 1.1. Map A shows the area represented by a multi-dimensional hillshade. The black dashed line shows a railroad track that cuts through the area. Map B shows the same area but represented by the roughness calculation, with a window radius of 35 cells. The light purple lines map the existing river terraces of the nearby Mississippi River. Map C shows the roughness map B with a hillshade added to it. This map highlights the natural grain of sediments within each terrace with thin black lines. Map D is a generic cartoon made to show the difference of sediment grain within each terrace deposit.

Chapter 4 Discussion

Previous studies have shown that the RF exhibits approximately 12 km of dextral offset at seismogenic depth, but only about 6 km of dextral offset across the surface expression, Reelfoot Scarp (Figure 1.3) (Pratt et al., 2013). This differential offset presents a large strain imbalance across the NMSZ system. Pratt (2012) hypothesized that part of the AF may continue past the intersection with RF further to the northeast, accommodating through-going transpressional strain. Evidence for transpressional faulting cross-cutting the RF could be a potential solution for the kinematic discrepancy. Woolery and Almayahi (2014) and Greenwood et al. (2016) subsequently found evidence supporting the idea of a through-going shear zone. Woolery and Almayahi (2014) completed a site characterization study at the CUSSO borehole and found near-vertical, transpressional style faulting in Paleozoic to basal Quaternary formations 12 km northeast of RF (Figure 1.2). The array aperture of the P-waves surveys was designed to image the Paleozoic bedrock (585 m) and consequently, could not resolve the upper 50 m of the surface. These transpressional faults are within the northwestern margin of Pratt et al.'s projected area for through-going shear and share spatial and architectural style consistent with the hypothesis. Woolery and Almayahi (2014) correlated the deformation and scale of fault with a lower-resolution industry seismic line 22 km to the northeast at Wolf Island, MO. This correlation suggests that the shear zone could potentially continue past Sassafras Ridge 22 km further to the northeast. Late-Quaternary displacement along the faults imaged at depth would need evidence or this interpretation is equivocal. A study completed by Greenwood et al. (2016) searched for the piercing point of the through-going shear zone of the AF with the RF. They imaged faults using seismic reflection, along the intersection of RF with CGF and RRF. One profile from this study revealed a near-

vertical, southwest dipping thrust fault which displaced Paleozoic-Eocene horizons. Another profile from Greenwood et al. (2016) imaged a north-dipping reverse fault which was defined as the southern margin of the Tiptonville dome. However, fault strike trends show that there is no apparent right-lateral offset of the RF and its hanging-wall (Tiptonville Dome) across CG and RR faults. Therefore, the piercing point is not at this structural intersection.

Rosandich (2019) investigated another potential piercing point of the AF through RF near Proctor City, TN with seismic reflection. The results showed steeply dipping, northeast-oriented, transpressional faults that uplifted and arched post-Paleozoic reflectors, extending into intra-Quaternary sediments. The faults imaged showed vertical displacement of 50 m, 16 m, and 5 m at the top of the Paleozoic, the top of the Eocene, the basal Quaternary gravel, respectively. Through back azimuth projection of the fault strikes at Proctor City, TN, Rosandich (2019) determined the faults are along strike with those imaged to the northeast by Woolery and Almayahi (2014). Rosandich (2019) concluded that this site is a likely piercing point for the through-going shear zone of the AF through RF, showing transpressional fault deformation into Quaternary sediments. This potential piercing point is located adjacent to where Chiu and Johnston (1992) defined the topographic segmentation of the RF into Reelfoot North and Reelfoot South, showing 5.5 km of lateral offset. In order to suggest the faults imaged at Sassafras Ridge by Woolery and Almayahi (2014) are a continuation of the transpressional structure imaged across RF (Rosandich, 2019) late-Quaternary displacement must be shown to satisfy the temporal boundary conditions. Correlation of Quaternary-active faults at Proctor City and Phillipy road with Quaternary-active faults at Sassafras Ridge is necessary for Pratt et al.'s (2012) hypothesis of a through going shear zone across the RF to remain valid. Correlation of the two fault zone would also suggest that the faults at Sassafras Ridge are a 12

km extension of the shear zone, accommodating motion of the RF throughout Quaternary time. The UK-1b seismic line was compared with Woolery and Almayahi's (2014) UK-1a line to show the spatial relationship of the transpressional faults imaged in deeper stratigraphy with their near-surface extension (Figure 4.1).

Our seismic reflection work confirms the faults imaged in deeper stratigraphy by Woolery and Almayahi (2014) show displacement across late-Quaternary sediments, representing transpressional deformation that reaches within 5 meters of the surface. The faults imaged show deformation within the Quaternary sediments and through surface terrain LiDAR analysis are thought to be expressed as a lineament along Sassafras Ridge. There is a set of atleast five transpressional faults in two zones of deformation that present vertical offset across late-Quaternary sediment horizons. The vertical displacement is approximately 10 m at the basal gravel to approximately 5 m at the boundary between coarse and fine sands ($\sim$ 10 m depth). We also were able to resolve a fault reaching within 5 m of the surface, offsetting the western boundary of a channel feature. Cooper (2016) collected an ER survey coincident with UK-1 investigating the Claiborne aquifer system in the upper part of the Mississippi Embayment. Cooper (2016) utilized surface ER with seismic walkaways to better understand the hydrostatic units of the shallow subsurface (Cooper, 2016). We were able to correlate the deformation we saw in the seismic profile UK-1b with deformation within the ER survey collected by Cooper (2016), suggesting that the deformation we see at depth extends to less than 5 m from the surface (Cooper, 2016). The ER survey provides imaging ability between 5 m depth and the surface, where our seismic survey was unable to image. Correlation of the seismic data with roughness maps shows that the 100 m area of fault deformation is coincident with the lineament imaged in a slope map of a roughness map (35-cell smoothing window)(Figure 3.7). These data provide evidence for right-lateral strike-slip faults that have continued 12 km northeast from

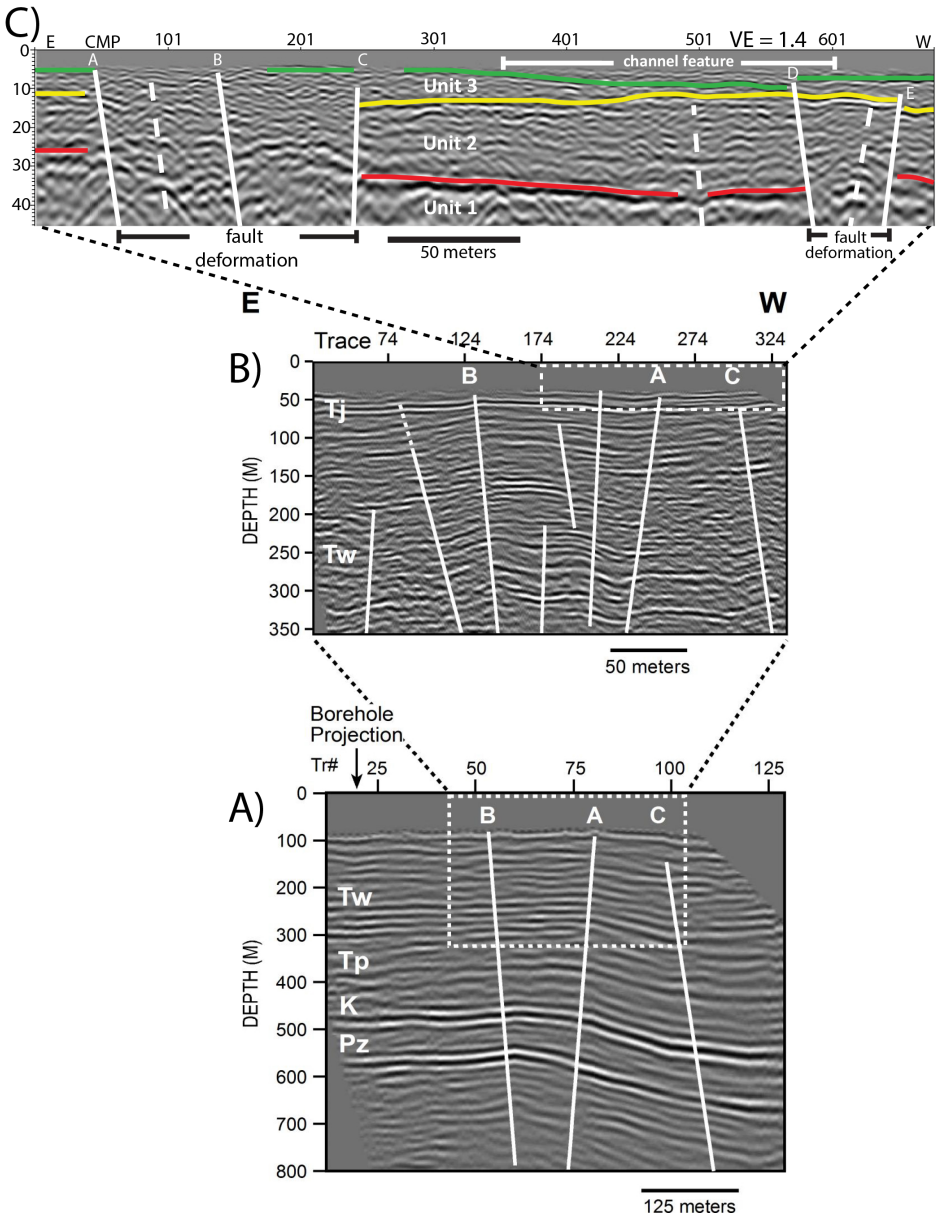

Figure 4.1: The spatial relationship between UK-1 (A) and UK-1a (B) Woolery and Almayahi (2014) with the UK-1b SH-wave data (C). UK-1b's array aperture was designed to target intra-Quaternary sediments within the unresolved depths of UK-1a (<50m). UK-1b was collected coincident with UK-1a, using a shorter array spacing to better image shallow Quaternary sediments and structure within the zone defined by the white dashed rectangle in B).

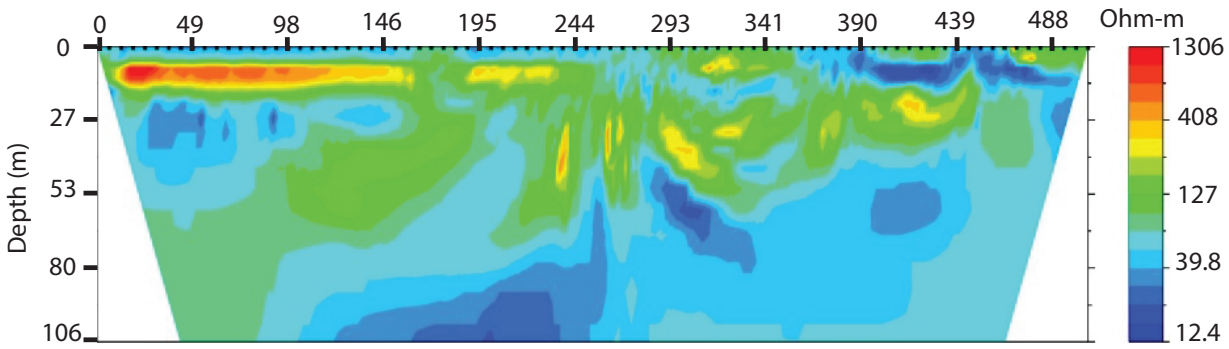

Figure 4.2: Electrical Resitivity survey collected by Cooper (2016). This survey shows that deformation is continuous within the upper 5 meters of the subsurface, between 380-480 feet along the survey.

the piercing point of the AF with the RF step-over, and based on digital terrain LiDAR analysis have surface expression representing a lineament that runs the length of Sassafras Ridge. The correlation of the SH-wave seismic data and relative temporal characteristics of surface features derived from LiDAR analysis present evidence that the interpreted faults are Quaternary-active and reach the surface within assumed Quaternary-aged, Mississippi River floodplain sediments.

Our findings support the hypothesis of right-lateral strike-slip faults that are accommodating displacement across the RF, allowing for movement to be continued across RF (Pratt, 2012). The interpretations also identify a new seismic hazard in the central U.S.A., presenting a previously unknown late-Quaternary-active fault system. This identification of these late-Quaternary faults provide a reduction for the seismic hazard uncertainty within the central U.S.A., through identifying a 12 km extension of the AF. Data from this work, correlated with P-wave seismic data presented by Woolery and Almayahi (2014) complete the characterization of faulting scale and mechanisms for the Sassafras Ridge faults, from Paleozoic horizons to the surface.

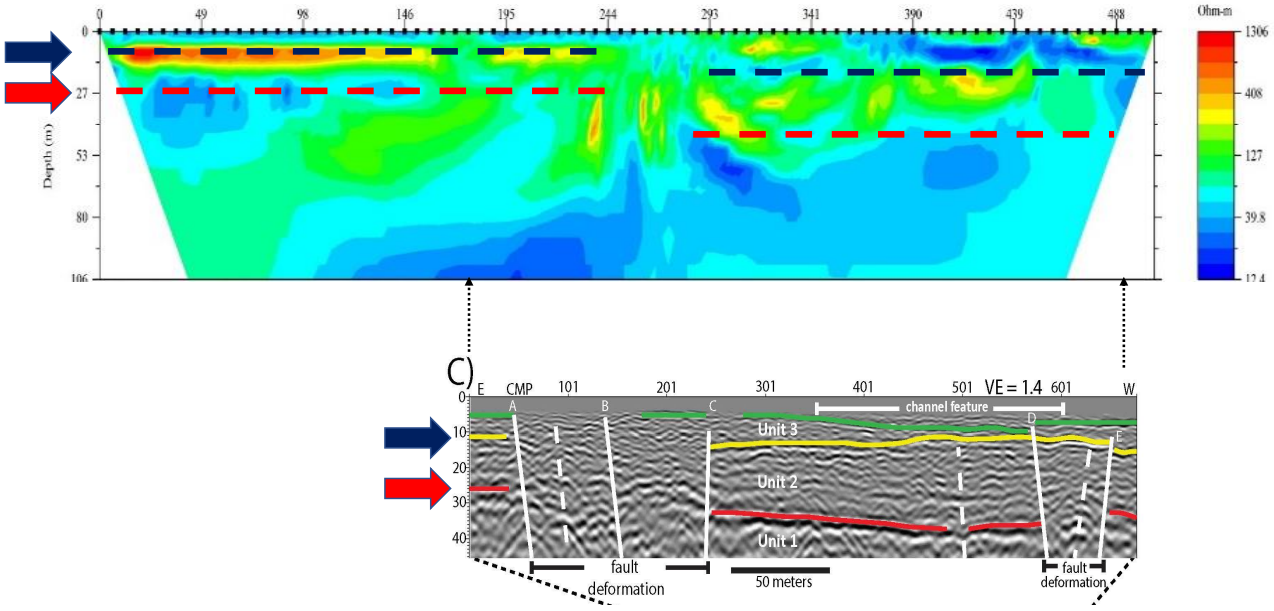

Figure 4.3: Spatial relationship between UK-1b seismic line and the ER surevy from Cooper (2016). Red dashed line shows the top of Unit 1 and the dark blue dashed line shows the top of Unit 2 in the ER.

Additional investigation of Wolf Island with near-surface SH-wave seismic surveys, showing transpressional displacement across Quaternary sediments would further support the hypothesis of the through-going shear zone (Woolery and Almayahi, 2014). Late-Quaternary evidence of fault displacement at Wolf Island would lengthen the extension of the fault zone to approximately 46 km. More so, this work could be furthered through acquisition of absolute age dates of each reflecting horizon imaged in UK-1b. Acquiring absolute age dates would allow for calculation of key seismic characteristics such as slip rate and provide a more constrained temporal scale of the mechanisms within the fault zone. Acquiring absolute age dates on the sediment within the adjacent terrace deposits (Figure 3.5; Terraces C, F, D2, and E1) would further constrain the temporal scale for the manifestation of the surface expression of these faults. The collection of Ground-Penetrating Radar (GPR) could prove beneficial across Sassafras Ridge and allow for geophysical imaging in the upper 5 m of the subsurface with amendable conditions. GPR has the ability to provide more

resolution of the upper 5 m where SH-wave seismic imaging was unable to resolve. Furthermore, trenching and sediment mapping within the trench would add information to further characterize and constrain the transpressional faults imaged all the way to the surface.

Chapter 5 Conclusions

Two transpressional fault zones 12 km to the northeast of Reelfoot Scarp and above previously identified deformation (Figure 3.4) were imaged with SH-wave seismic reflection, and supported by digital terrain LiDAR analysis, are Quaternary active. The largest of these deformation zones is ∼100 m wide and contains atleast three interpreted, near-vertical, dextral strike-slip faults, showing transpressional displacement. Discontinuous reflectors, antiforms, and diffraction patterns indicate deformation associated with these faults reaches within 5 m of the surface. The basal Quaternary gravel layer is vertically offset by these faults by atleast 9 m. Shallower at 11 m depth, intra-Quaternary sediment horizons show atleast 4 m of vertical offset. Faults C and D in UK-1b are the near-surface extent of faults A and C in UK-1a, respectively. These faults are imaged reaching to 5 m depth. Faults A and C form a graben defining the boundaries of the 100 m fault zone; structurally consistent with near-surface flower structures and Pratt et al.'s hypothesis of the shear zone (Pratt, 2012). The faults imaged within the deep stratigraphy profiles (UK-1 and UK-1a)(Woolery and Almayahi, 2014) continue into Quaternary sediments and show displacement of intra-Quaternary sediments. There is a second, slightly smaller zone of deformation (∼50m wide) in the western margin of line UK-1b, showing two near-vertical, transpressional faults (D and E). These faults show similar characteristics to the fault strands imaged at depth (Woolery and Almayahi, 2014) and displace intra-Quaternary sediments as well. These faults also define the margins of a small graben while offsetting the basal Quaternary gravel by ∼5 m. The vertical displacement of shallower Quaternary sediments shows ∼4 m. Vertical offset across the western margin of the channel feature is ∼3 m at 8 m depth. The intra-Quaternary coarse sands unit (Unit 2) shows sediment thickening to the west and indicates syndepositional faulting within the Quaternary

time. Surficial terrain LiDAR analysis supports the conclusion that the 100m wide deformation zone is coincident with the subtle pressure ridges of Sassafras Ridge. Sassafras Ridge's western margin is consistent with fluvial terrace deposits of the Mississippi River showing a steep, arcuit, "nose-shaped" slope. The sediment grain within the deposit is cross-cut by a lineament with subtle pressure ridges bounding each side. The lineament and associated pressure ridge are aligned with the largest area of near-surface fault deformation and is likely a surficial expression of the faults imaged at depth.

The displacement of late-Quaternary sediments by transpressional faulting indicates an approximately 12-km-long Quaternary-active northeastern extension of a through-going shear zone of the AF across and northeast of the RF. Fault trends at Sassafras Ridge are in line with transpressional faults imaged at the structural intersection of the AF with RF (Rosandich, 2019). The transpressional faults at Sassafras Ridge are a continuation of the Quaternary-active structure imaged at Proctor City, TN (Rosandich, 2019). Temporal correlation with the similar, deeper structure imaged at Wolf Island, MO (Woolery and Almayahi, 2014) could indicate the shear zone could extend as far as 46 km to the northeast of RF. The extension to Sassafras Ridge is an ∼300-m-wide zone of fault strands characterized as an transpressional flower structure bounded by near-vertical, compressional and dextral faults in the shallow subsurface. The structure is consisted with findings of previous studies (Woolery and Almayahi, 2014; Rosandich, 2019) as well as analogous kinematic models of deformation above strike-slip faults (Pratt, 2012). The faults at Sassfras Ridge provide a possible solution to the strain imbalance seen across RF, and demonstrate that the AF extension continues to accommodate right-lateral motion continuously through time with only a percentage of motion being expressed as vertical or horizontal displacement of the RF (Pratt, 2012).

The findings of this study offer further clarity on seismic hazard sources for the NMSZ through identification of Quaternary-active faulting that was not previously discovered. The uncertainty in seismic hazard assessment in the area is reduced through characterization of the degree of faulting and defining an extension of a large and historically active fault segment. These results further the neotectonic characterization of the area northeast of RF and can provide information for future fault modeling. Integration of near-surface seismic imaging with digital terrain LiDAR analysis provides an advantageous way to define near-surface faults and their relationship with surficial features.

Bibliography

Baker, G. S. (1999). *Processing near-surface seismic-reflection data: A primer*. SEG Books.

Burger, H. R., Sheehan, A. F., and Jones, Craig H & Burger, H. R. (2006). *Introduction to applied geophysics: Exploring the shallow subsurface*, volume 550. WW Norton New York.

Calais, E., Freed, A., and Van Arsdale, R & Stein, S. (2010). Triggering of new madrid seismicity by late-pleistocene erosion. *Nature*, 466(7306):608–611.

Calais, E., Mattioli, G., DeMets, C., Nocquet, J.-M., Stein, S., and Newman, A & Rydelek, P. (2005). Tectonic strain in plate interiors? *Nature*, 438(7070):E9–E10.

Calais, E. and Stein, S. (2009). Time-variable deformation in the new madrid seismic zone. *Science*, 323(5920):1442–1442.

Chiu, J. and Johnston, AC & Yang, Y. (1992). Imaging the active faults of the central new madrid seismic zone using panda array data. *Seismological Research Letters*, 63(3):375–393.

Cooper, M. (2016). Integrated geophysical methods in investigation of claiborne aquifer hydrostratigraphy, jackson purchase, kentucky. *Master's Thesis, Theses and Dissertations–Earth and Environmental Sciences*, 37.

Cox, R. T., Van Arsdale, R. B., Harris, J. B., Forman, S. L., and Beard, William & Galluzzi, J. (2000). Quaternary faulting in the southern mississippi embayment and implications for tectonics and seismicity in an intraplate setting. *Geological Society of America Bulletin*, 112(11):1724–1735.

Crone, A. J. (1998). Defining the southwestern end of the blytheville arch, northeastern arkansas: Delimiting a seismic source zone in the new madrid region. *Seismological Research Letters*, 69(4):350–358.

Crone, A. J., McKeown, F. A., Harding, S. T., Hamilton, R. M., and Russ, David P & Zoback, M. D. (1985). Structure of the new madrid seismic source zone in southeastern missouri and northeastern arkansas. *Geology*, 13(8):547–550.

Csontos, R. and Van Arsdale, R. (2008). New madrid seismic zone fault geometry. *Geosphere*, 4(5):802–813.

Csontos, R., Van Arsdale, R., and Cox, Randel & Waldron, B. (2008). Reelfoot rift and its impact on quaternary deformation in the central mississippi river valley. *Geosphere*, 4(1):145–158.

Dix, C. H. (1955). Seismic velocities from surface measurements. *Geophysics*, 20(1):68–86.

Ervin, C. P. and McGinnis, L. (1975). Reelfoot rift: Reactivated precursor to the mississippi embayment. *Geological Society of America Bulletin*, 86(9):1287–1295.

Frankel, A. (1995). Mapping seismic hazard in the central and eastern united states. *Seismological Research Letters*, 66(4):8–21.

Frankel, K. L. and Dolan, J. F. (2007). Characterizing arid region alluvial fan surface roughness with airborne laser swath mapping digital topographic data. *Journal of Geophysical Research: Earth Surface*, 112(F2).

Greenwood, M. L., Woolery, E. W., Van Arsdale, R. B., and Stephenson, William J & Patterson, G. L. (2016). Continuity of the reelfoot fault across the cottonwood grove and ridgely faults of the new madrid seismic zone. *Bulletin of the Seismological Society of America*, 106(6):2674–2685.

Grohmann, C. H., Smith, M. J., and Riccomini, C. (2010). Multiscale analysis of topographic surface roughness in the midland valley, scotland. *IEEE Transactions on Geoscience and Remote Sensing*, 49(4):1200–1213.

Hamilton, R., Zoback, M., and McKeown, FA & Pakiser, L. (1982). Tectonic features of the new madrid seismic zone from seismic-reflection profiles. *Investigations of the New Madrid, Missouri, Earthquake Region*, 1236:55–82.

Harding, T. P. (1985). Seismic characteristics and identification of negative flower structures, positive flower structures, and positive structural inversion. *AAPG bulletin*, 69(4):582–600.

Harris, J. B. (1996). Shear-wave splitting in quaternary sediments: Neotectonic implications in the central new madrid seismic zone. *Geophysics*, 61(6):1871–1882.

Herrmann, R. B. and Canas, J.-A. (1978). Focal mechanism studies in the new madrid seismic zone. *Bulletin of the Seismological Society of America*, 68(4):1095–1102.

Howe, J. R. and Thompson, T. L. (1984). Tectonics, sedimentation, and hydrocarbon potential of the reelfoot rift. *Oil & Gas Journal*, 82(46):179–190.

Hunter, J., Pullan, S., Burns, R., and Gagne, RM & Good, R. (1984). Shallow seismic reflection mapping of the overburden-bedrock interface with the engineering seismograph—some simple techniques. *Geophysics*, 49(8):1381–1385.

Johnston, A. C. and Schweig, E. S. (1996). The enigma of the new madrid earthquakes of 1811–1812. *Annual Review of Earth and Planetary Sciences*, 24(1):339–384.

Langenheim, V. E. (1995). *Gravity of the New Madrid seismic zone: A preliminary study*, volume 1538. US Government Printing Office.

Lillie, R. J. (1999). Whole earth geophysics. *An Introductory Textbook for Geologists*.

Lindsay, J. B. and Newman, D. R. (2018). Hyper-scale analysis of surface roughness. *PeerJ Preprints*, 6:e27110v1.

Newman, A., Stein, S., Weber, J., Engeln, J., and Mao, Ailin & Dixon, T. (1999). Slow deformation and lower seismic hazard at the new madrid seismic zone. *Science*, 284(5414):619–621.

Nuttli, O. W. (1973). The mississippi valley earthquakes of 1811 and 1812: Intesities, ground motion and magnitudes. *Bulletin of the Seismological Society of America*, 63(1):227–248.

Odum, J. K., Stephenson, W. J., and Shedlock, Kaye M & Pratt, T. L. (1998). Near-surface structural model for deformation associated with the february 7, 1812, new madrid, missouri, earthquake. *Geological Society of America Bulletin*, 110(2):149–162.

Parrish, S. and Van Arsdale, R. (2004). Faulting along the southeastern margin of the reelfoot rift in northwestern tennessee revealed in deep seismic-reflection profiles. *Seismological Research Letters*, 75(6):784–793.

Pratt, T. L. (1994). How old is the new madrid seismic zone? *Seismological Research Letters*, 65(2):172–179.

Pratt, T. L. (2012). Kinematics of the new madrid seismic zone, central united states, based on stepover models. *Geology*, 40(4):371–374.

Pratt, T. L., Williams, R., and Odum, Jackson K & Stephenson, W. J. (2013). Origin of the blytheville arch, and long-term displacement on the new madrid seismic zone, central united states. *GSA Special Papers*, 493:1–15.

Pryne, D., Van Arsdale, R., and Csontos, Ryan & Woolery, E. (2013). Northeastern extension of the new madrid north fault, new madrid seismic zone, central united states. *Bulletin of the Seismological Society of America*, 103(4):2277–2294.

Rhea, S. and Wheeler, R. L. (1994). Map showing large structures interpreted from geophysical data in the vicinity of new madrid, missouri. Technical report, US Geological Survey.

Rosandich, B. (2019). Extension of a quaternary-active shear zone across the reelfoot fault. *Master's Thesis, Theses and Dissertations–Earth and Environmental Sciences*, 79.

Schweig, E. S. and Ellis, M. A. (1994). Reconciling short recurrence intervals with minor deformation in the new madrid seismic zone. *Science*, 264(5163):1308–1311.

Sheriff, R. E. and Geldart, L. P. (1995). *Exploration seismology*. Cambridge university press.

Smalley, R., Ellis, M., and Paul, J & Van Arsdale, R. (2005). Space geodetic evidence for rapid strain rates in the new madrid seismic zone of central usa. *Nature*, 435(7045):1088–1090.

Tuttle, M. P., Schweig, E. S., Sims, J. D., Lafferty, R. H., and Wolf, Lorraine W & Haynes, M. L. (2002). The earthquake potential of the new madrid seismic zone. *Bulletin of the Seismological Society of America*, 92(6):2080–2089.

Van Arsdale, R. (2000). Displacement history and slip rate on the reelfoot fault of the new madrid seismic zone. *Engineering Geology*, 55(4):219–226.

Van Arsdale, R. B. and TenBrink, R. K. (2000). Late cretaceous and cenozoic geology of the new madrid seismic zone. *Bulletin of the Seismological Society of America*, 90(2):345–356.

Wang, Z. and Carpenter, N Seth & Woolery, E. W. (2019). Horizontal-to-vertical spectral ratio of s-waves and sh-wave transfer functions at the vertical seismic and strong-motion arrays in the central united states. *Journal of Applied Geophysics*, 162:64–71.

Widess, M. (1973). How thin is a thin bed? *Geophysics*, 38(6):1176–1180.

Woolery, E. W. and Almayahi, A. (2014). Northeast-oriented transpression structure in the northern new madrid seismic zone: Extension of a shear zone across the reelfoot fault stepover arm. *Bulletin of the Seismological Society of America*, 104(5):2587–2596.

Woolery, E. W. and Street, R. (2002). Quaternary fault reactivation in the fluorspar area fault complex of western kentucky: Evidence from shallow sh-wave reflection profiles. *Seismological Research Letters*, 73(5):628–639.

Woolery, E. W., Street, R. L., and Wang, Zhenming & Harris, J. B. (1993). Near-surface deformation in the new madrid seismic zone as imaged by high resolution sh-wave seismic methods. *Geophysical Research Letters*, 20(15):1615–1618.

Woolery, E. W., Wang, Z., Seth Carpenter, N., and Street, Ron & Brengman, C. (2016). The central united states seismic observatory: Site characterization, instrumentation, and recordings. *Seismological Research Letters*, 87(1):215–228.

Woolery, E. W., Wang, Z., and Street, Ron L & Harris, J. B. (1996). Ap-and sh-wave seismic reflection investigation of the kentucky bend scarp in the new madrid seismic zone. *Seismological Research Letters*, 67(2):67–74.

Yilmaz, Ö. (2001). *Seismic data analysis: Processing, inversion, and interpretation of seismic data*. Society of exploration geophysicists.

Cooper Cearley VITA

Education:

- Millsaps College, Geophysics BS, 2019

Career:

- ITS Helpdesk Analyst - Millsaps College (2016-2019)
- Teaching Assistant - University of Kentucky (2019-2021)

Awards:

- Co-Director of Research Symposium for Earth and Environmental Sciences (ReSEES), 2020
- Excellence on Comprehensive Exams, Millsaps College, 2019
- Mississippi Geological Society Lawrence F. Boland Scholarship, Millsaps College, 2019
- Third Place Undergraduate Presentation, Mississippi Academy of Sciences, 2018, 2019
- Top Presentation, Beta Beta Beta Science Symposium, Millsaps College, 2018

Conference Presentations and Publications:

- Vanderlip, C. A., Cox, R. T., Larsen, D., Mitchell, J., Harris, J. B., and Cearley, C. S., 2021, "Newly Recognized Quaternary Surface Faulting and Folding Peripheral to the New Madrid Seismic Zone, Central U.S., and Implications for Restraining Bend Models of Intraplate Seismic Zones", The Journal of Geology, v. 129, in press.

- Analysis of the Kingtown Lineament (Phillips County, Arkansas) Using Integrated Seismic Reflection and Ground-Penetrating Radar Data" Presenter. American Geophysical Union Conference, Washington D.C. December 2018.

- Preliminary Seismic Investigation of the Bliss Creek Lineament near Edwards, Mississippi" Presenter. Beta Beta Beta Student Research Symposium, Millsaps College. February 2018.

- Preliminary Seismic Investigation of the Bliss Creek Lineament near Edwards, Mississippi" Presenter. Mississippi Academy of Sciences Conference, Hattiesburg, Mississippi. February 2018.

- Near-Surface Geophysical Imaging of Deformation Associated with the Daytona Beach Sand Blow Deposits, Lee County, Arkansas." Co-Author. American Geophysical Union Conference, New Orleans, LA. December 2017.